The Thesis Committee for Thomas Joseph Goller
Certifies that this is the approved version of the following Thesis:

Simultaneous High-Speed Displacement and Surface Pressure Measurements of a Compliant Panel under a Mach 2 Compression Ramp Interaction

APPROVED BY
SUPERVISING COMMITTEE:

Noel T. Clemens, Supervisor

Jayant Sirohi

Simultaneous High-Speed Displacement and Surface Pressure Measurements of a Compliant Panel under a Mach 2 Compression Ramp Interaction

by

Thomas Joseph Goller

Thesis

Presented to the Faculty of the Graduate School of

The University of Texas at Austin

in Partial Fulfillment

of the Requirements

for the Degree of

Master of Science in Engineering

The University of Texas at Austin

May 2019

Dedication

I would like to dedicate this work to my parents and my brother, who have always provided endless love, support and guidance throughout all of my pursuits. You have taught me to always strive for quality, and it is because of you that I am able to do what I love and live a blessed life.

Acknowledgements

The work presented in this thesis is a result of the collaborative efforts of many individuals, without whom it would not have been possible. Mustafa Musta provided assistance in designing and executing experiments as well as analysis of data. Daiju Uehara contributed his expertise in the digital image correlation measurement method. Leon Vanstone offered constant guidance with data acquisition methods, implementation and general knowledge. Jeremy Jagodzinski supervised the operation of the wind tunnel at the J.J. Pickle Research Campus and was always available to answer any laboratory or design-related questions to ensure the success of the experiments. Additional thanks to Lee Mears and Dr. Farrukh Alvi from Florida State University for their efforts in helping to develop the pressure-sensitive paint recipe and to Sandia National Laboratories for sponsoring this work.

Lastly, advisor Dr. Noel Clemens and co-advisor Dr. Jayant Sirohi provided endless expertise, knowledge and guidance that gave me the opportunity to learn, grow and become a better scientist. Their time and support in this project was paramount to its success.

Abstract

Simultaneous High-Speed Displacement and Surface Pressure Measurements of a Compliant Panel under a Mach 2 Compression Ramp Interaction

Thomas Joseph Goller, M.S.E.

The University of Texas at Austin, 2019

Supervisor: Noel T. Clemens

In this presentation we will discuss a new study of the dynamic response of a compliant panel under a shock wave/boundary layer interaction produced by a compression ramp in a Mach 2 flow. The experiments were conducted in the High-Speed Wind Tunnel at the J.J. Pickle Research Campus at The University of Texas at Austin. The tunnel has a cross-sectional area of 150 mm by 150 mm, and the compliant panel is 127 mm by 68 mm and located at the spanwise centerline of the floor of the test section. The compliant panels are made of polycarbonate and have thicknesses of 2 mm, 1.5 mm and 1 mm. The compression ramp, which was located at the downstream end of the compliant panel, has a 20 degree compression angle and is 102 mm wide and 28 mm high. Side fences were used to maintain quasi-two dimensionality of the mean separated flow. Fast-response (Kulite) pressure transducers were located immediately upstream of the compliant panel. The primary measurements that will be reported are simultaneous surface displacements by using the stereo digital image correlation (DIC) technique, and fast pressure sensitive

paint (PSP). Both techniques were performed at 6.4 kilohertz acquisition rates. The DIC gives the displacement of the compliant panel in the vertical direction, and the PSP gives the surface pressure over the entire panel. The combination of pressure and displacement measurements allows the characterization of the structural response of the panel due to the unsteady pressure loading caused by the shock-induced turbulent separated flow.

Table of Contents

List of Tables

List of Figures

CHAPTER 1

Introduction

Fluid-structure interactions (FSIs) have become a major focus area of research efforts in recent years. Concerns with shock wave-boundary layer interactions (SWBLIs) on high-speed aircraft have garnered much attention, as the effects are not well understood. The importance of understanding the potential severe acoustic, thermal and structural consequences of these SWBLIs is exacerbated by thin structures that are subjected to them (McNamara and Friedmann [2011]). The low frequency unsteady pressure fluctuations of the interactions tend to overlap with the resonant frequency modes of thin aerostructures, resulting in a two-way fluid-structure coupling. This aerodynamic environment can lead to very strong dynamic loading, large deformations, fatigue and even failure as a result (Brouwer et al. [2017]).

Many efforts have been made to simulate the interactions using computational models, and many more have attempted to gain understanding through extensive experimental testing (Beardsell [2016]; Clemens [2014]; Daub [2016]; Dussauge [2006]; Pham [2018]; Spottswood [2012]; Xiaolin [2018]). A goal from these collaborative efforts is to understand the characteristics of supersonic and hypersonic FSIs in order to be able to possibly predict the pressure-forcing an aircraft structure may experience and design for

that environment accordingly. The structures can then be tailored to alleviate detrimental effects and perhaps even use them for a practical gain (Pham et al. [2018]).

Studying SWBLIs does not come without its complications, however. In the case of experimental testing, obtaining accurate and non-intrusive time-resolved measurements of the unsteady flow structure presents numerous challenges. Some methods have been developed to obtain measurements of the surface pressure on a structure under the shock foot and separation region without disrupting the incoming boundary layer, as well as structure movement without the need for physical transducers (Casper [2016]; Davis [2015]; Lynch [2018]; Whalen [2019]).

The purpose of this work is to further explore the high-speed flow-structure coupling of a compliant panel subjected to a SWBLI from a compression ramp interaction. Through experimental testing, the ultimate objective is to acquire simultaneous measurements of both the flow and the dynamic response of the panel. Techniques that are implemented include digital image correlation (DIC), pressure sensitive paint (PSP) to measure panel displacement and surface pressure, respectively. All tests presented here were run at a free stream Mach number of 2.

CHAPTER 2

Literature Review

2.1 QUALITATIVE SUMMARY OF SHOCK WAVE-BOUNDARY LAYER INTERACTIONS AND UNSTEADINESS

Shock wave-boundary layer interactions are unavoidable when aircraft are moving at supersonic velocities, and the design of high-speed vehicles is complicated by the challenges in modeling such interactions (Spottswood et al. [2012]). The unsteady pressure and heat transfer loading caused by SWBLIs can lead to decreased vehicle performance and structural integrity.

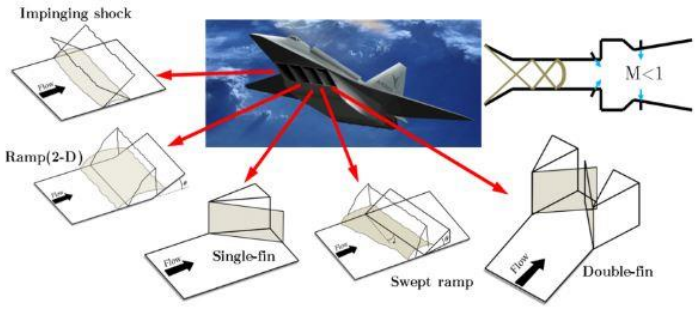

Figure 1 Several types of ramp and fin-induced shock wave-boundary layer interactions. (Gaitonde [2015])

Figure 2.1.2 shows a more detailed diagram of a compression ramp SWBLI, where the supersonic flow turns to the ramp geometry by means of a shock wave. The impinging

separation shock intersects with the incoming turbulent boundary layer. The shock foot is the location where the separation shock meets the wall. The range of shock foot motion is signified by $l_{i,}$ which is a result of the shock unsteadiness. Downstream of the separation shock foot, the boundary layer thickens and a region of separated flow forms, designated by L_{sep}.

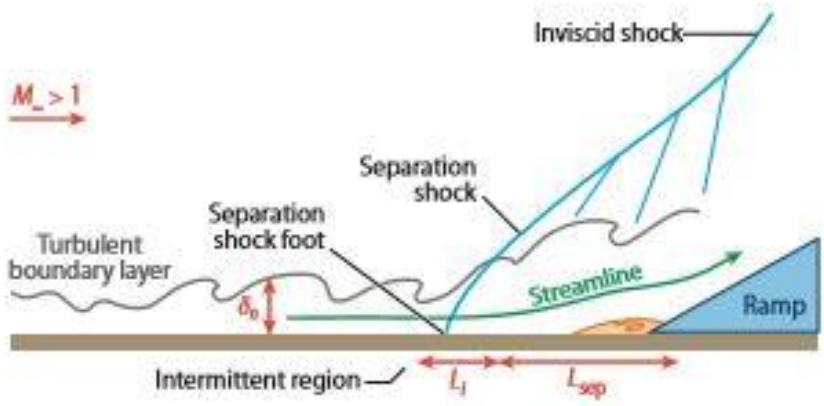

Figure 2 Diagram of compression ramp shock wave-boundary layer interaction. (Clemens and Narayanaswamy [2014])

For a compression ramp interaction, the flow compresses as it approaches the obstruction, and in the supersonic regime, it generates an oblique shock wave. The flow far from the wall experiences a pressure rise across the shock that is similar to that experienced by an inviscid shock with the same ramp angle. Alternatively, the boundary layer flow close to the wall is more severely affected by the presence of the shock and can become separated downstream of the shock foot. In the separation region, the flow exhibits a thin bubble where the flow recirculates. Schlieren imaging of the flow features of the ramp flow

geometry is detailed in Figure 2.1.3, where flow separation and reattachment are clearly visible.

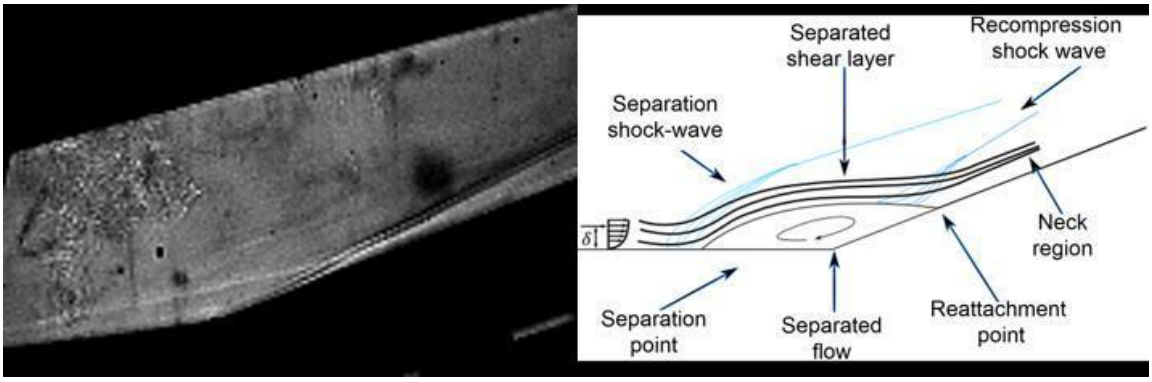

Figure 3 Schlieren image and diagram of ramp-induced SWBLI. (Martos [2017])

The work presented in this thesis focuses on the interaction generated by an unswept compression ramp in a Mach 2 flow. In the unswept ramp the mean flow is largely two-dimensional, although the flow is highly three-dimensional instantaneously.

One of the most important characteristics of SWBLIs is the unsteadiness of the separated flow. The separation bubble behind the shock interaction “breathes” in response to the coupled upstream and downstream movement of the shock impingement and separation locations (Whalen et al. [2019]). A larger separation occurs when the separation location is further upstream than the overall mean location. The frequency of these unsteady oscillations is considerably lower than the characteristic frequencies of turbulence in the incoming boundary layer (Dolling 1993). These frequencies can be low enough – less than 10 kHz – that they can overlap with the modal frequencies of thin structures on a vehicle, and the unsteadiness imparts a dynamic load which can excite those modes.

2.2 IMPINGING SHOCK OSCILLATIONS OF SHOCK WAVE-BOUNDARY LAYER INTERACTIONS

While extensive work has been conducted to understand the cause of the low-frequency unsteadiness of separated SWBLIs, there is no current consensus on the cause of the unsteadiness or breathing motion of the shock foot. Dussauge et al. [2005] conducted an experimental study of a reflected shock at Mach 2.3 in order to find an origin of low frequency motions of the shock fluctuation. In a comparison of pressure power spectral densities (PSDs) of low frequency content at the shock foot and the recirculation region in Figure 2.2.1, it was remarked that in the recirculation region, the frequencies were in the same range as that of shock motion. The shock motion was estimated to represent about 25 percent of the total energy, indicating there is a link between the two. They concluded that eddies in the downstream separation region may be the source of the shock excitation and that the shock itself acts as a low pass filter, where it only allows the low frequency section to be excited.

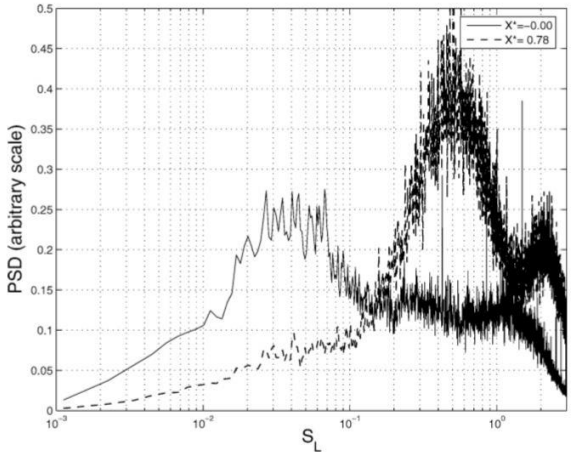

Figure 4 Power spectral density of pressure fluctuations at shock foot ($X^* = 0$) and recirculation region ($X^* = 0.78$). (Daussage et al. [2005])

However, they were not left without unanswered questions. According to the study, the oscillations of the wind tunnel itself were simply assumed to be out of the shock oscillation frequency range, but they were not checked. If there were excitations intrinsic to the wind tunnel, it would reduce the validity of the interpretations. Another issue that arose was the dependence of the flow structures on downstream boundary conditions. Any 3-dimensional vortices downstream of the test area could have similar time scales to the shock motion frequencies, so the question is posed as to whether there is a connection between the SWBLI and downstream structures.

Whalen et al. [2019] looked at turbulent boundary layer measurements in a ramp-induced SWBLI of various angles at Mach 6 to observe boundary layer disturbances and separation length. This setup is shown in Figure 2.2.2. Wall pressure distributions were obtained, as well as flow field visualization using schlieren imaging. It was found that for high ramp angles (strong shocks), pressure measurements indicated large amplification of disturbances and also revealed shock foot motion frequencies.

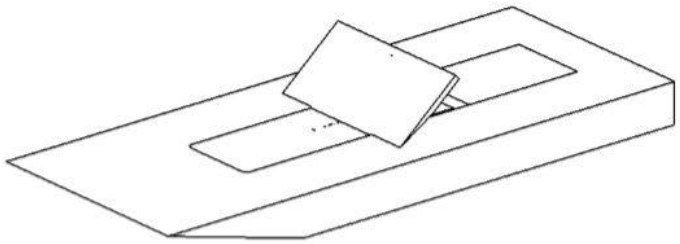

Figure 5 Experimental model of flat plate with variable angle ramp. (Whalen et al. [2019])

Identified in Figure 2.2.3, schlieren imaging exposed convection of instabilities into the interaction, which produced smaller “shocklets.” These shocklets were correlated with the instantaneous separation length through both the pressure measurements and schlieren. Therefore, the presence of the shocklets propagating through the turbulent separated interaction suggests that there is a correlation with large instantaneous separation lengths.

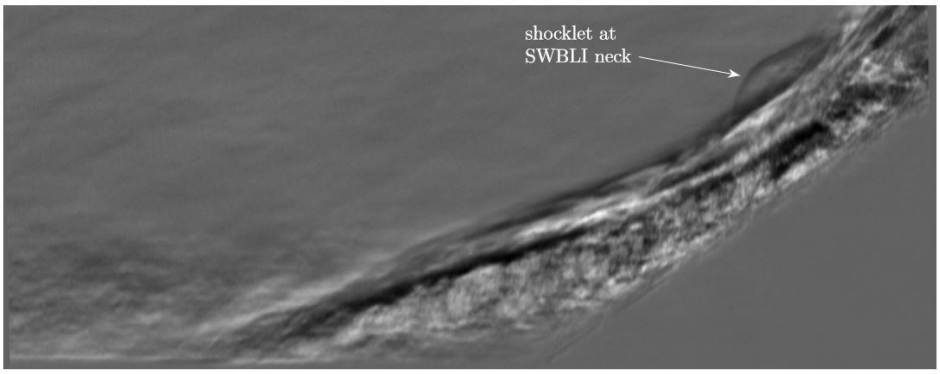

Figure 6 Schlieren image of shocklet convecting through the SWBLI. (Whalen et al. [2019])

Xiaolin et al. [2018] carried out an investigation into the unsteadiness of a SWBLI in a compression ramp interaction at Mach 6 as well. The compression ramp angles were varied, and they found that the reattachment shock decreases with increasing ramp angle, and the influence area of the unsteadiness expands with increasing ramp angle. Characteristic frequencies of 320 kHz were found within the interaction area for a 22 degree ramp. The amplitude of power spectrum peaks increased with increasing Reynolds number, and analysis of the pressure confirmed a nonlinear nature of the unsteadiness within the SWBLI.

2.3 NUMERICAL APPROACH TO SHOCK WAVE-BOUNDARY LAYER INTERACTIONS AND THIN STRUCTURE COUPLING

It is relatively well-understood how shock waves interact with solid, rigid structures due to the lack of compliance that would normally result in large local pressure variations. However, when the structures are much more lightweight and flexible, as is often case in the design of aircraft, they can respond in very unpredictable ways. The responses to the aerodynamic loads are not the result of a single phenomenon. Rather, it is a coupled system involving both the fluid and the structure whose effects influence one another. Many simulations and experiments have been carried out in an attempt to determine the likely dominant driving forces involved in the SWBLI on a compliant surface, some of which will be discussed in this section as well as the following one.

As a method to better model boundary conditions of the flexible surface, Visbal [2012] used a numerical approach with the full conservative compressible Navier-Stokes equations with curvilinear coordinate transformation, allowing for a deforming mesh. Visbal studied panel flutter unsteadiness and its coupling with a shock reflection system of various strengths. The solver also employed a solution to the non-linear Karman plate equations. The pressure on the underside of the panel was set to the mean theoretical value that was to be expected on the top. Results showed that for sufficiently strong shocks, oscillation amplitudes and frequencies of the panel increased with increasing shock strength (Figure 2.3.1), and the fluttering panel propagates pressure fluctuations along the reflected shock system. The critical dynamic pressure at which panel flutter onset occurs decreased with increasing shock strength, but it was also found to decrease to a value lower

than the critical dynamic pressure for the case of flutter with no shock. This suggested another type of aeroelastic instability is present and is a consequence of the shock interaction, but further analysis is needed to examine the effects of the shock impingement location and other variables.

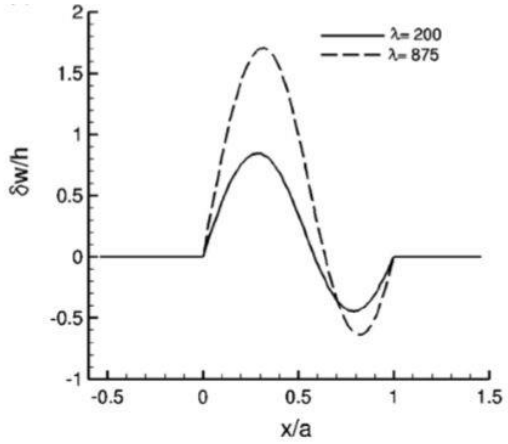

Figure 7 Effect of dynamic pressure on panel dynamics. Higher pressure correlates to higher amplitudes. (Visbal [2012])

In a follow-up paper, Visbal [2014] furthered his study and employed the same numerical solver techniques to observe the effects of shock impingement location and cavity pressure on the panel dynamics. Additional conclusions from this newer study found that significant changes in the panel dynamics do occur as a function of the shock impingement location and controlled cavity pressure. As the shock impingement location on the panel is moved upstream towards the leading edge, panel oscillations were significantly diminished and a steady static deformation was present. However, as the location neared the leading edge, those oscillations reemerged. Figure 2.3.2.a illustrates the static deformation solutions of various shock impingement locations, and Figure 2.3.2.b shows the frequency spectra of those locations. At locations x_i/a = 0.38 and 0.25, the

oscillations are nearly nonexistent, but close to the leading edge at $x_i/a = 0.18$, the spectral peak reemerges at a higher frequency.

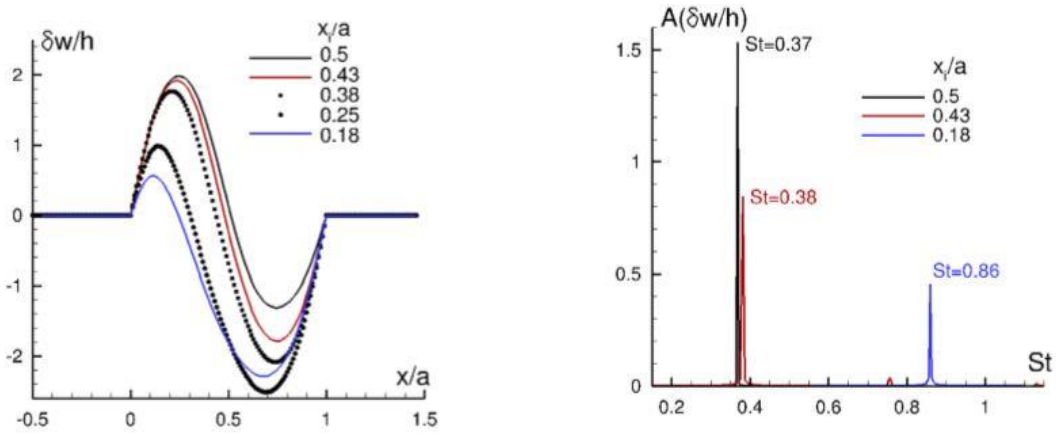

(a) (b)

Figure 8 Effect of shock impingement location on panel dynamics – (a) time-averaged panel deflection and (b) oscillation frequency spectra. (Visbal [2014])

The cavity pressure was tested at 3 different values: the theoretical pressures for upstream of the incident shock ($p_c/p_1 = 1.0$), downstream of the shock ($p_c/p_1 = 1.4$), and averaged ($p_c/p_1 = 1.2$). With both the higher and lower values, a steady buckled solution was achieved, whereas in the averaged case limit-cycle oscillations were obtained, as shown in Figure 2.3.3. This implies that forced panel oscillations can be induced by specified cavity pressures, thereby reducing flow separation caused by the shock interaction.

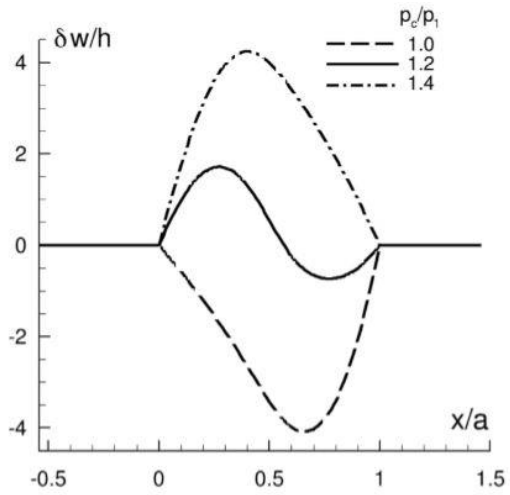

Figure 9 Effect of cavity pressure on panel dynamics. (Visbal [2014])

The findings in Visbal's [2014] study certainly suggest that aeroelastically-tailored flexible panels can be used as a means of passive flow control. Self-excited oscillations arise from specific cavity backpressure and shock impingement locations, resulting in the reduction of time-averaged separation regions.

A numerical study of an impinging shock on a compliant surface was conducted by Brouwer et al. [2017] who compared changes in the separation bubble size and surface pressure for both static and unsteady pressure loading cases. They used an implicit finite volume Reynolds-averaged Navier-Stokes (RANS) solver. The results revealed that the size of the separation bubble varied greatly with the static surface deformation, which resulted in large changes in the aerodynamic forces on the panel. Additionally, the odd-numbered modes of the surface deformation produced much larger separated flow regions than the even-numbered modes (see Figure 2.3.4). These observations were largely attributed to the curvature of the panel. As the frequency of panel motion increased, the

separation length amplitude was found to decrease, which was attributed to the forcing of the flow resulting in panel motion. Brouwer et al. acknowledged that, due to the nature of the solver implemented and assumptions made, there is a lot of room for improvement before these high-fidelity flows can reliably and accurately simulate the complexity of the SWBLIs with a compliant surface.

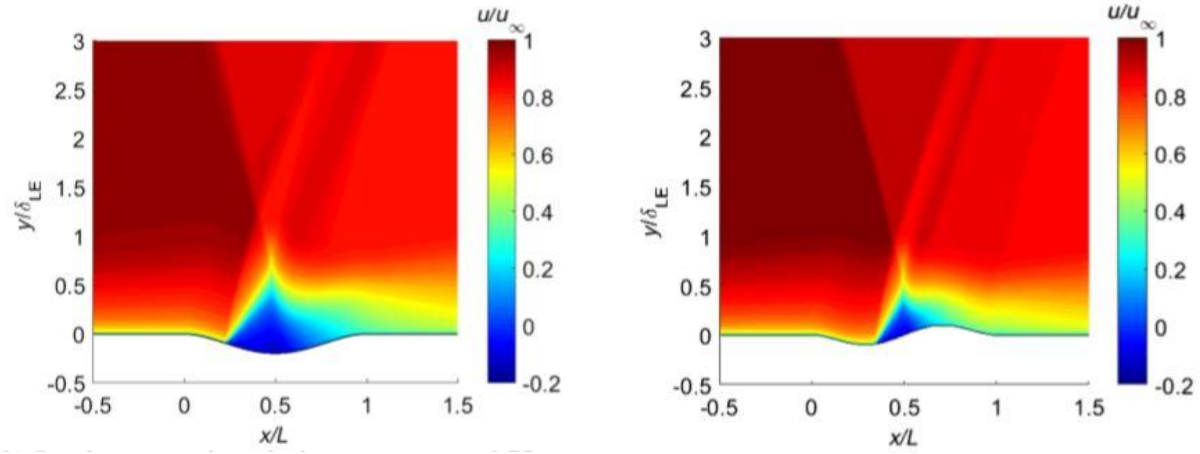

Figure 10 Steady streamwise velocity contours for (a) mode 1 panel oscillations and (b) mode 2 panel oscillations. (Brouwer et al. [2017])

Although numerical simulations are useful in helping to better understand SWBLIs, they are not truly representative of the real world due to many assumptions and approximations that are made. For this reason, experimental testing has been chosen as the method by which these interactions are studied in this thesis.

2.4 EXPERIMENTAL EFFORTS IN SHOCK WAVE-BOUNDARY LAYER INTERACTIONS WITH COMPLIANT SURFACES

Daub et al. [2016] conducted a study on a coupled FSI from an impinging shock using conventional measurement techniques – high-speed pressure transducers and capacitive displacement sensors. A unique feature of this experiment was their ability to move the shock location during the wind tunnel run, where the quick change of the impingement point on the elastic panel was used to excite high-amplitude oscillations. The panel was designed to have vibrational modes in the range of the low-frequency movements of the separation shock. Kulite pressure transducers measured the pressure distribution on the panel, and the results for various shock angles at Mach 4 are shown in Figure 2.4.1. The effect of shock angle and impingement location on the panel pressure distribution can be seen quite clearly, where the stronger interactions move further upstream and produce larger pressure rises across the shock.

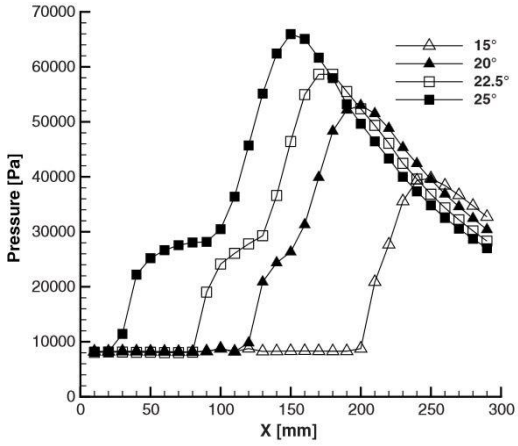

Figure 11 Static pressure distribution at Mach 4 for different fixed shock angles. (Daub et al. [2016])

For the tests where the ramp angle was actuated from 0 to 20 degrees in 10 ms, capacitive sensors recorded the displacement of the panel at locations near the front, center,

and rear of the panel. Figure 2.4.2.a shows the strong agreement between two separate runs, suggesting repeatability and no plastic deformation, in addition to the transient displacements of the panel resulting from the change in incident shock angle. For a fixed shock angle, oscillation is excited by the flowfield and the panel has both static and dynamic influence on the separation region. In Figure 2.4.2(b), power spectral densities of all three capacitive sensor locations detail reasonable agreement as well.

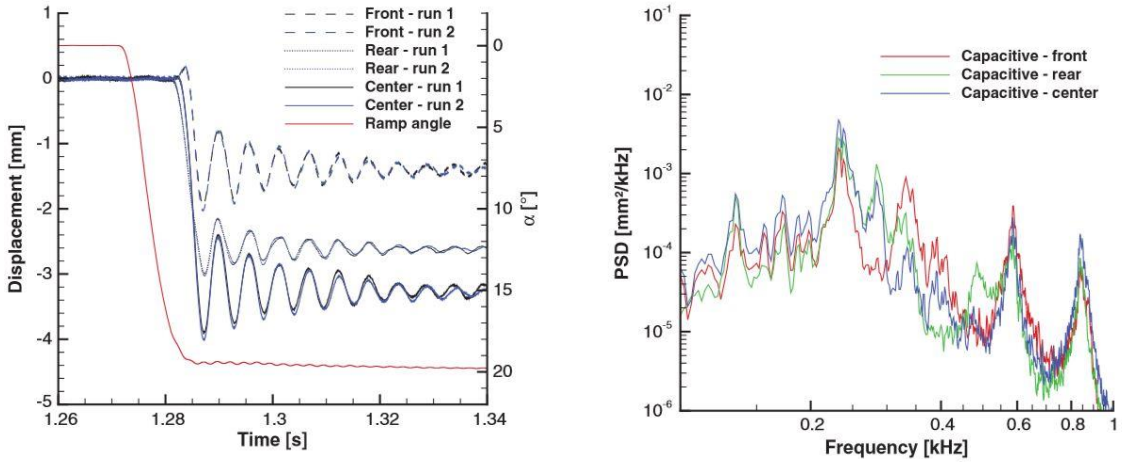

(a) (b)

Figure 12 Elastic panel dynamics – (a) capacitive sensor displacements for shock angle rotation to 20 degrees and (b) PSD at different panel locations for constant shock angle. (Daub et al. [2016])

One problem with conventional instrumentation is that the use of physical transducers and sensors imparts added mass to the panel, thereby altering the structural dynamics and eigenmodes that it was originally designed for. This drawback can be

eliminated by the use of alternate non-intrusive pressure and deformation measurement techniques.

An experimental study by Beardsell et al. [2016] measured the motion of a 1/16" thick polycarbonate compliant surface subjected to an impinging shock in a Ludwieg tube. As opposed to the previous pressure transducer and capacitive sensor methods, measurements were made using a single-point laser displacement sensor (LDS) and single-camera diffraction-assisted 3D digital image correlation (DAIC). Preliminary findings from controlled *ex situ* tests showed that the LDS can resolve modal frequencies over 1 kHz and amplitudes as small as 1 μm, whereas the DAIC gave less precise data, but with the advantage of obtaining full field measurements. One challenge that was encountered with the LDS was the apparent discretization of the acquired displacement data. It was hypothesized that the laser beam from the sensor reflects off of the deformed, non-perpendicular surface and back into a different CCD pixel in the sensor. A schematic of this effect is shown in Figure 2.4.3.

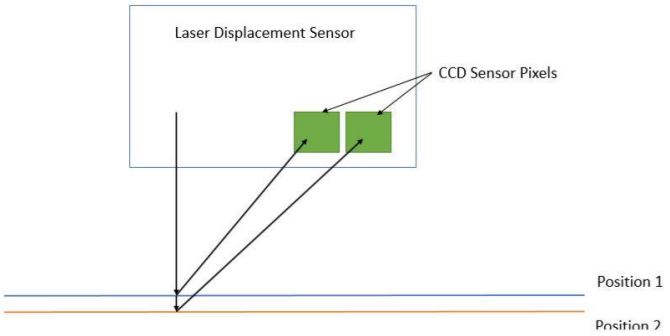

Figure 13 Laser beam offset due to changing panel position. (Beardsell et al. [2016])

This is believed to cause the sudden jumps in the data as the sensor records a change in position when the laser beam changes pixels. However, the overall positive results prove that this can be an effective tool in measuring surface deformation and serve as a valuable validation method for the full-field DAIC measurements.

Spottswood et al. [2012] used digital image correlation (DIC) to measure full-field panel surface deformations as well, but they also simultaneously implemented high-speed pressure-sensitive paint (PSP) to measure surface pressure distribution as an alternative to traditional pressure transducers. The panel design and setup was similar to that used by Daub et al., with a thin steel panel having multiple eigenmodes below 500 Hz and a movable shock generator. In this case the cavity pressure under the panel was equalized to reduce tunnel startup loading and a rigid panel was used as a control. Several tests were performed at different fixed shock impingement locations, and it was observed that the panel response is very sensitive to small changes in impingement location, depicted in Figure 2.4.4. As the location was moved from near the center of the panel to near the leading edge, the magnitude of certain modal frequency modes were amplified while others were mitigated.

Also shown in Figure 2.4.4 is the pressure distribution obtained from the PSP. When a shock is present, there is roughly a two-fold increase in pressure on the panel. It is noted that there were difficulties with the implementation of the PSP. The paint application resulted in an uneven surface finish and required a large amount of smoothing of the raw PSP images. Also, the camera setup was misaligned, causing bad calibration and noisy

images for the no shock cases. However, there is still qualitative evidence of fluid-structure coupling.

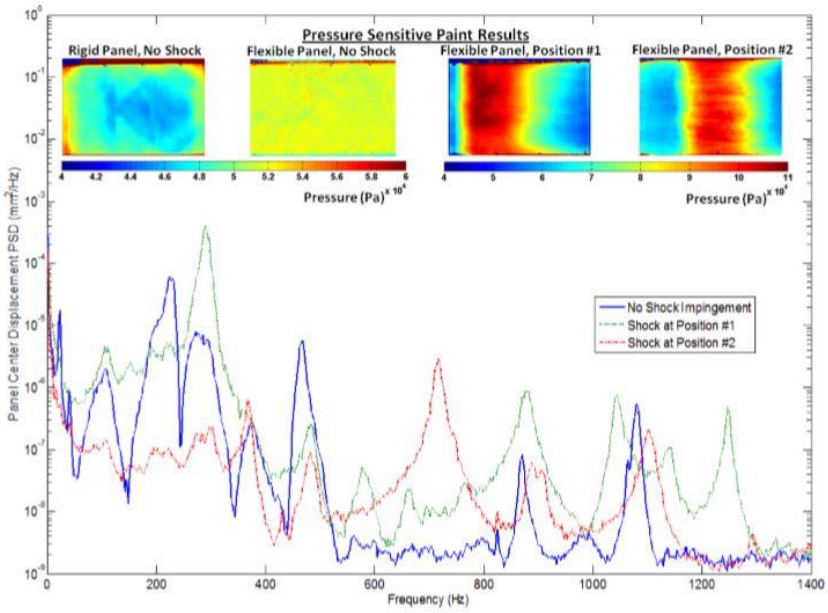

Figure 14 PSD of panel center displacement and time-averaged surface pressure distributions for different shock locations. (Spottswood et al. [2012])

Spottswood et al. also considered a single heated flow test case to induce static and dynamics instabilities resulting from the fluctuating pressure. More analysis is required, but preliminary results in Figure 2.4.5 show no shift in the dominant modal frequencies when the flow was heated. There is broadening of the first peak, which may suggest that a nonlinear response is present. However, due to additional damping it could still be linear. Overall, full-field high-speed dynamic pressure and deformation response data were acquired simultaneously, evidencing the usefulness of these methods in aiding to further understand FSIs. However, only the displacement and pressure responses of the panel are

discussed. In the work presented in this thesis, those responses are also correlated with the movement of the shock foot oscillations to further explore the fluid-structure coupling.

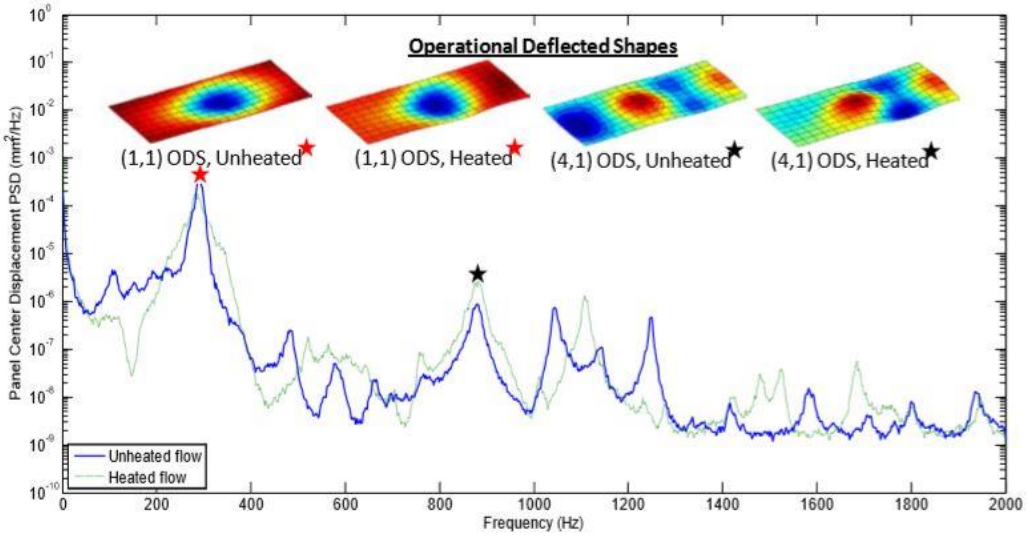

Figure 15 PSD of panel center displacement and deflected-shape response for unheated and heated flow cases. (Spottswood et al. [2012])

Flexible panels are not the only specimen that have been studied as an attempt to better understand these SWBLIs. Pham et al. [2018] proposed an investigation into a class of FSIs that involves an unsteady shock wave on a “soft” surface, rather than a solely flexible one. An important distinction between the two is that the soft panels deform locally under stress without large structural responses, whereas a flexible panel does not. Surface flow visualizations were taken of a soft rubber insert under a compression ramp interaction. Pressure transducer measurements were also taken and compared to those taken from a rigid panel test case.

Results indicated that the presence of the soft rubber insert reduced the size of the separation region. Figure 2.4.6 shows the comparison of the soft compliant surface (top) to the rigid plate (bottom) for different shock strengths. There is a clear reduction in separation size, and the reduction is greater for stronger shocks. Figure 2.4.7 shows the PSD of the pressure obtained within the intermittent region for both the compliant and rigid cases. There is a large reduction of about 40 to 50 percent of the energy content in the unsteady frequency range below 1 kHz. It is also noted that the frequency at which maximum energy content occurs shifted higher for the compliant panel compared to the rigid panel. This is consistent with the reduction in separation sizes seen in Figure 2.4.6.

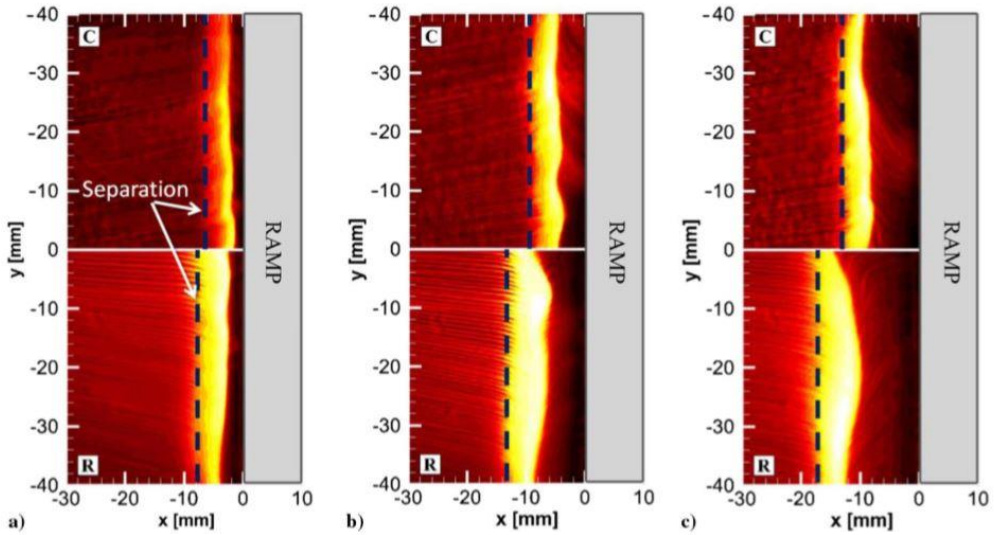

Figure 16 Comparison of surface flow visualizations and separation regions for rubber surface (top) and rigid surface (bottom) at compression ramp angles of (a) 16 degrees, (b) 20 degrees and (c) 24 degrees. (Pham et al. [2018])

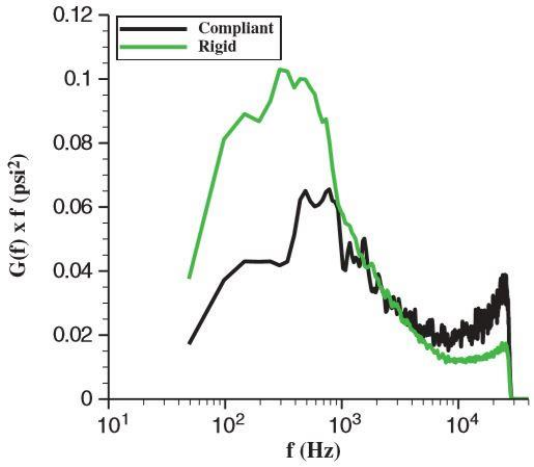

Figure 17 Pressure PSD comparison of rubber compliant surface and rigid surface within the intermittent region at compression ramp angle of 20 degrees. (Pham et al. [2018])

The question remains as to what the exact mechanisms are that contributed to the reduction in the mean separation size and low-frequency energy content in the SWBLI over the soft rubber surface. However, it looks promising that using soft materials in locations where FSIs are expected can indeed mitigate unsteady shock loading, even by as much as 50 percent.

It is generally accepted that there is a coupling between the responses of the compliant surface and the shock interaction. Many different approaches, both computational and experimental, have been implemented in a collective effort to ascertain the characteristics and mechanisms involved in these complex fluid-structure interactions. In terms of experimental techniques, several different pressure and deformation measurement methods were used with varying degrees of success. For the work presented

in the remainder of this thesis, the previously described PSP and DIC methods will be further explored.

2.5 PRESSURE-SENSITIVE PAINT, DIGITAL IMAGE CORRELATION AND PARTICLE IMAGE VELOCIMETRY

A different approach of studying fluid-structure interactions was taken by Lynch et al. [2018], where pressure and deformation measurements were taken of an impulse loading on a jointed beam structure inside a shock tube. Rather than traditional pressure sensors and strain gauges, non-invasive pressure-sensitive paint and stereo digital image correlation techniques were employed. The measurements were able to identify the structural modes of the beam, providing evidence that these can be powerful data acquisition techniques in the future study of FSIs.

Although several different recipes of PSP have been made with varying results, a common formulation is the fast-response porous PSP that uses a platinum-tetra-fluoro-phenyl-porphyrin (PtTFPP) luminophore with a polymer-ceramic (PC) binder. This includes a two-step paint application process in which the luminophore layer is sprayed on top of the PC binder layer. The luminophore absorbs excitation light at 400 nm and emits light near 650 nm. The paint works by way of oxygen quenching and the emission is inversely proportional to the partial pressure of oxygen. Wagner et al. [2017] and Casper et al. [2016] used this paint to study FSIs and claimed to be able to obtain a pressure frequency response of up to 10 kHz. They also performed an *in situ* calibration to the actual

pressure by varying the pressure within a sealed cavity and measuring the luminescence. Peng et al. [2016] used the same recipe as well, but reported a frequency response of up to only 6 kHz. All studies reported that the quality of the paint degraded over time and per wind tunnel run, and thus needed to be repainted fairly regularly. Results were overall within about 10 percent compared to pressure measurements taken from Kulite transducers. Temperature sensitivity effects were neglected for relatively low Mach numbers. An example trace comparison between the PSP and Kulites is shown in Figure 2.5.1.

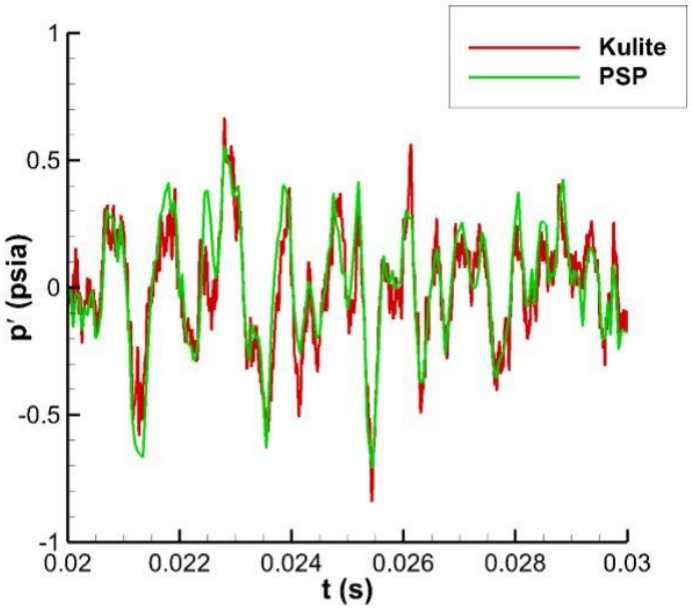

Figure 18 Pressure measurement trace comparison between PSP and Kulite transducers. (Casper et al. [2016])

Lynch et al. [2018] used stereo DIC for fluid-structure interactions in a shock tube at several different driver pressures. They applied a speckle pattern to the test subject using an ink stamp with 0.013 mm dot size. The grid was calibrated using a target, and images

were acquired at 20 kHz. The signals obtained from both the PSP and DIC were normalized to their respective *rms* values and compared in Figure 2.5.2. The phase and frequency between the PSP and DIC match very well and appear to be coupled. Spottswood et al. [2012] also implemented high-speed DIC, but hand-painted the speckle pattern using a fine-tipped marker. The acquisition rate in their shock generator setup was 4 kHz, and deflected mode shapes between the PSP and DIC taken at the center of the flexible panel were also found to correlate very well. The lower acquisition rates prove not to be a problem since the oscillations of the shock foot and modal frequencies of the panel are mostly less than 1 kHz, so they can be easily resolved.

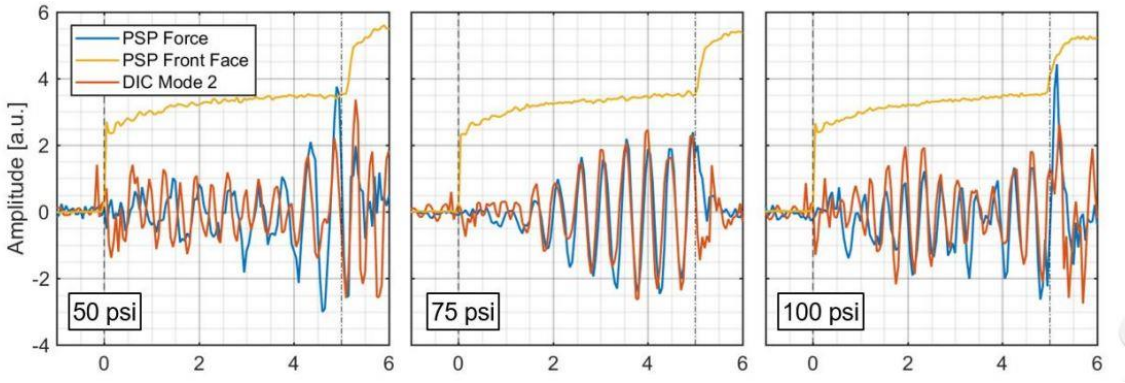

Figure 19 Time traces of PSP and DIC responses at different driver pressures. Dashed lines correspond to incident and reflected shocks. (Lynch et al. [2018])

Wagner et al. [2017], in addition to measuring pressure, also measured velocity in an open cavity flow using stereoscopic time-resolved PIV. Mineral oil was used as the seed particles, with an average particle diameter of about 0.8 μm. They used a 532 nm Nd:YAG laser with 40 mJ, 10.2 ms pulses. The thickness of the laser sheet was 2.0 mm, and two

cameras acquired images at 50 kHz. Mean and turbulence velocity fluctuations were successfully imaged with the installed PIV setup and vortices formed by the open cavity were visible. PSDs of the streamwise velocity at different spanwise locations are shown in Figure 2.5.3, where the peaks are well-aligned with the first three modal frequencies. It was observed that the amplitude increases towards the wall (indicated by red line). Additionally, significant variation in resonance dynamics were noted, suggesting that PIV can certainly be used to study structural responses in FSIs.

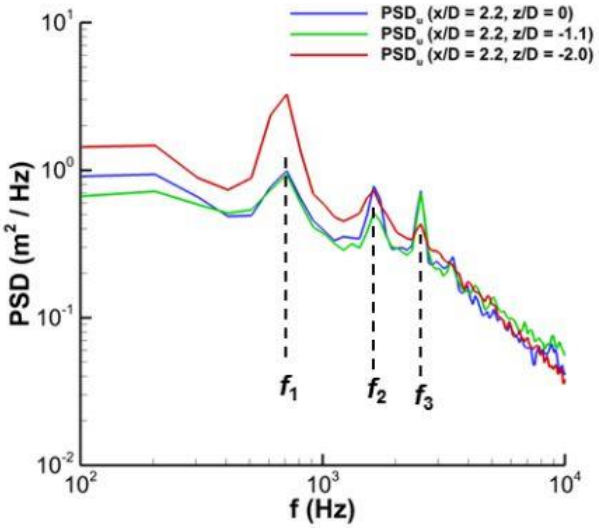

Figure 20 PSDs of streamwise velocity obtained from PIV at different spanwise cavity locations. First 3 modes indicated by dashed lines. (Wagner et al. [2017])

Employing all three techniques of PSP, DIC and PIV simultaneously to measure surface pressure, deformation and velocity, respectively, can perhaps prove to be an effective approach to reveal more information about the complex nature of fluid-structure interactions on a compliant surface. Although not included in the remainder of this thesis, PIV will be implemented in future work on this experiment.

CHAPTER 3

Experimental Procedures

3.1 WIND TUNNEL FACILITY

All experiments presented in this thesis were conducted at the high-speed blowdown wind tunnel at the J.J. Pickle Research Campus at The University of Texas at Austin. The wind tunnel can be fitted with nozzle blocks to produce either Mach 2 or Mach 5 flow conditions in the test section. For the purpose of this thesis, all tests were done at Mach 2 with future plans to rerun the tests at Mach 5. The tunnel has a rectangular test section with dimensions 6.3" (160 mm) high and 6" wide (152 mm). It is 30" (762 mm) long with the Mach 2 nozzle installed and 27" (685 mm) long with the Mach 5 nozzle installed. Additional operating test condition details for the Mach 2 tunnel are provided by Vanstone et al. [2017] and are displayed in Table 3.1.1.

Condition	Imperial Units	S.I. Units
Nominal M_∞	2	2.
Stagnation Pressure (P_0)	37.9 psia	261 kPa
Stagnation Temperature (T_0)	66° F	292 K
Free Stream Reynolds Number (Re)	1.16×10^7 ft^{-1}	3.8×10^7 m^{-1}
Boundary Layer Thickness (δ_{99})	0.45 in	11.75 mm

Table 1 Operating test conditions for Mach 2 wind tunnel.

For the tunnel equipped with the Mach 5 nozzle block, the incoming flow is heated upstream of the stagnation chamber. Operating test condition details for the Mach 5 tunnel are displayed in Table 3.1.2.

Condition	Imperial Units	S.I. Units
Nominal M_∞	4.91	4.91
Stagnation Pressure (P_0)	334 psia	2.30 MPa
Stagnation Temperature (T_0)	206° F	370 K
Free Stream Reynolds Number (Re)	1.52×10^9 ft^{-1}	5.0×10^9 m^{-1}
Boundary Layer Thickness (δ_{99})	.19 in	4.7 mm

Table 2 Operating test conditions for Mach 5 wind tunnel.

The tunnel uses 180 ft^3 (4 m^3) of compressed air at 2250 psia (15.5 MPa), giving a maximum runtime of approximately 30 seconds for Mach 2 and approximately 60 seconds for Mach 5. A detailed schematic of the wind tunnel section facility and a diagram of the tunnel section are also shown in Figure 3.1.1 and Figure 3.1.2, respectively. A door on one side of the test section allows access for installing tunnel components and models. Fused quartz or fused silica windows run the length of the test section on the ceiling and both sides, allowing optical access for setting up high-speed cameras, lasers and lights for use in data acquisition. Before measurements were taken during the tunnel run, some time was allotted for the tunnel to reach steady state and ensure it had started.

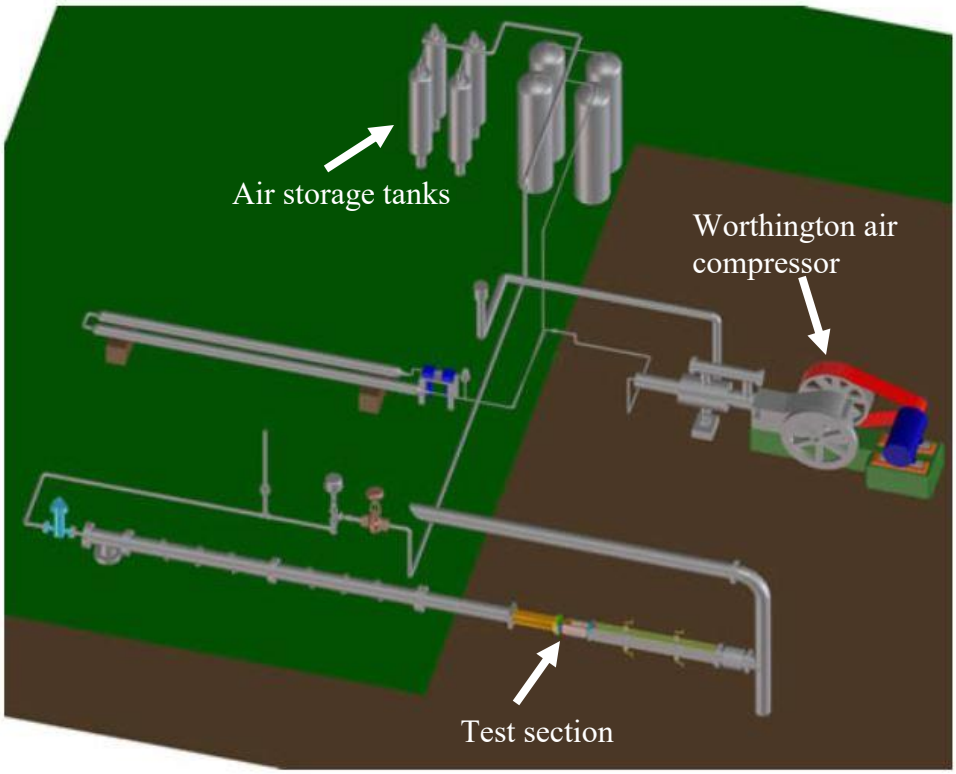

Figure 21 Schematic (not to scale) of the high-pressure system for the high-speed wind tunnel testing facility at the J.J. Pickle Research Campus. (Adapted from Eddie Zihlman)

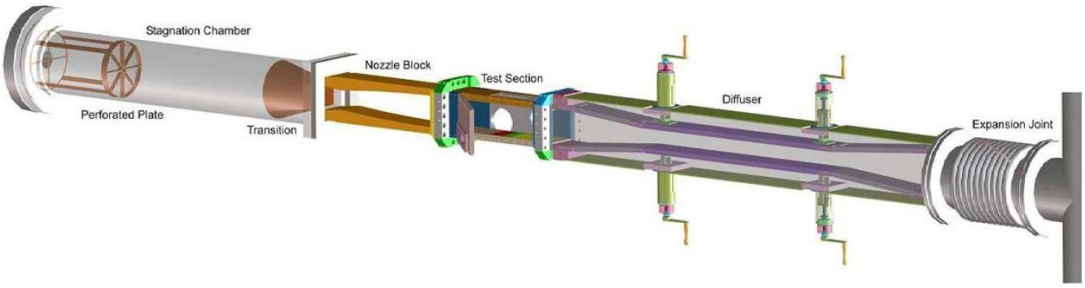

Figure 22 Schematic of the high-speed wind tunnel section at the J.J. Pickle Research Campus. (Austin [2001])

3.2 TEST MODEL DESIGN AND INSTALLATION

A floor plug was installed in the test section of the tunnel through a cutout in the floor and bolted from underneath. The floor plug can be modified to house a variety of test models to be inserted into the tunnel. For the experiments in this thesis, the floor was modified to have attachment points to secure a compression ramp, the compliant test panel, and five Kulite XCQ-062 pressure transducers. These transducers have a range of up to 50 psi (6.895 MPa), the sampling used frequency was 100 kHz. They were installed by first mounting the transducers in brass or stainless steel hollowed out 4-40 threaded screws, and they were inserted into the models by hand. All custom parts were manufactured using Aluminum 6061-T6, except for the panels, which were are of polycarbonate.

Figure 3.2.1 shows the floor plug and model setup. The compression ramp was bolted to the surface of the floor just downstream of the panel, and up to 5 pressure transducers can be installed just upstream of the panel. The transducers are located 0.25 *in* (6.35 mm) in front of the upstream edge of the panel, and the spanwise spacing is 0.4 *in* (10.16 mm) on center. Although up to 5 transducers can be installed, due to space limitations only 2 were used for most tests in measuring the incoming boundary layer pressure. The empty holes were filled with solid 4-40 threaded screws. The ramp is double sided with compression angles of 20 and 21 degrees and has a width of 4 *in* (10.16 mm) and a height of 1 *in* (25.4 mm). All of the tests presented here were done with the 20 degree angle. Not shown in Figure 3.2.1, but shown in Figure 3.2.2 are side fences on the ramp that extend 10 mm out from the leading edge.

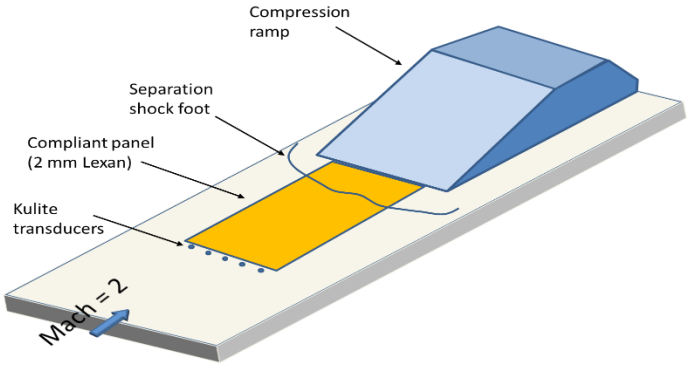

Figure 23 Installation of model components into wind tunnel floor. (Courtesy of Dr. Noel Clemens)

The bottom of the compliant panel is open and a 3” (76.2 mm) by 6.8” (172.7 mm) by 3/8” (9.5 mm) thick borosilicate glass window and frame is bolted from the underside of the tunnel through to the floor plug. This serves two distinct and important purposes – to create an environment sealed off from atmosphere so that the inside pressure under the panel surface can be controlled independently, and to allow optical access for DIC camera viewing. A model of this setup is displayed in Figure 3.2.2, and a picture viewing the underside is shown in Figure 3.2.3. A vacuum pump can be connected to the window cavity using Swagelok® connectors and a ball valve, allowing control of the cavity pressure. For the Mach 2 tests, it was intended to set the pressure to approximately the static pressure of the flow, about 7 psi (48.3 kPa). The purpose of this was to attempt to equalize the pressure on the top and bottom of the panel in order to have an effective mean deflection of zero. However, due to the nature of an unsteady SWBLI, a true zero mean is not possible. It is also worth noting that the actual pressure in the cavity fluctuated slightly during the run due to small leaks in the seals.

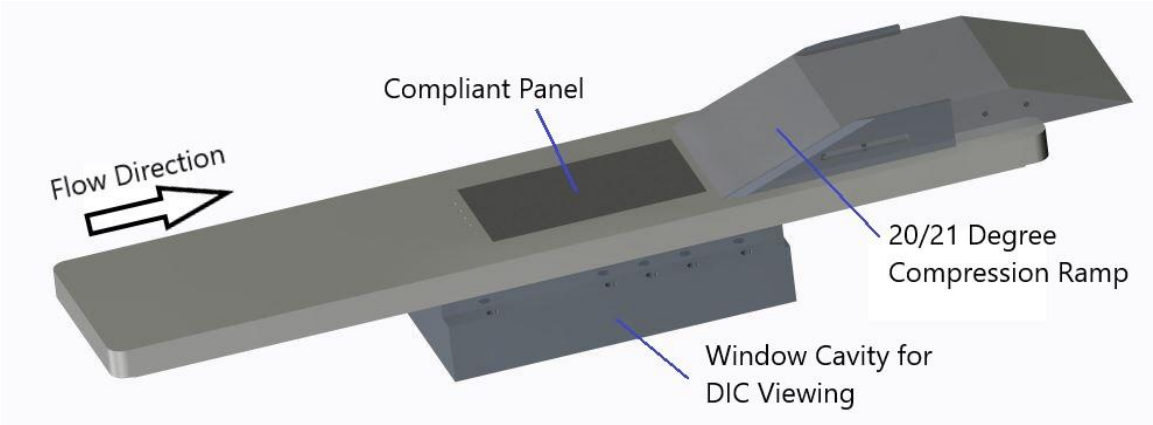

Figure 24 Schematic of the tunnel floor showing placement of window allowing DIC camera access.

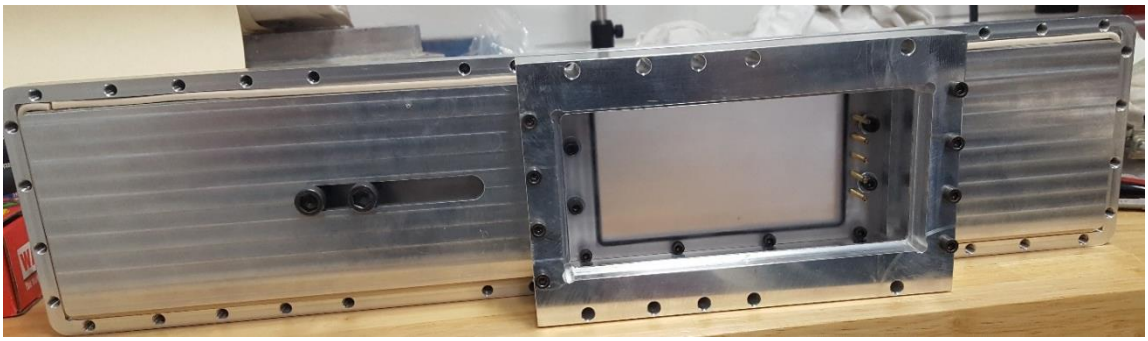

Figure 25 Photograph of the bottom of assembled floor model highlighting underside view of panel through window.

The compliant panel, mounted with small screws from the underside of the floor, is flush to the flow side of the tunnel floor and sealed with an O-ring. The panel is assumed to have rigid constraints on all sides and have no movement with respect to the tunnel on the edges. The test panels are 5.2 *in* (132.1 mm) by 2.9 *in* (73.7 mm) with 0.1” *in* (2.54 mm) wall thickness. This gives effective panel dimensions of 5” (127 mm) by 2.7 *in* (68.6

mm) with square corners. There are 5 holes on the upstream flange to allow installation of the pressure transducers. A model of the panel is shown in Figure 3.2.4.

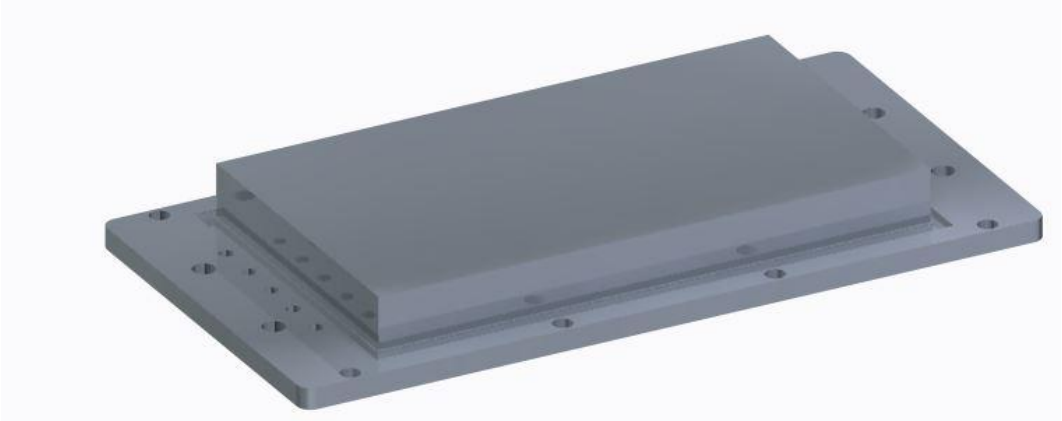

Figure 26 Rendered model of polycarbonate compliant test panel.

In this study, various panel thicknesses were used – 2 mm, 1.5 mm and 1 mm. These thicknesses were chosen based on the resonant frequencies of the first few modes of the structure, as outlined in Table 3.2.1. These theoretical modal frequencies were determined by a rectangular plate with clamped boundary conditions on all sides using Equation 3.1 (Blevins [1979]).

$$f = \frac{\lambda^2}{2\pi a^2}\left[\frac{Eh^3}{12\gamma(1-\nu^2)}\right]^{1/2} \tag{3.1}$$

In Equation 3.1, f is the modal frequency, λ is dimensionless parameter that is a function of the mode number, a is the plate length, b is the plate width, h is the plate thickness, E is the modulus of elasticity of polycarbonate (2.1 GPa), γ is the mass per unit area of the plate and ν is Poisson's ratio of polycarbonate (0.33). The frequencies were

intentionally designed to be in the range of shock foot oscillation. In addition to the compliant panels, a non-compliant rigid panel was machined, installed and tested as a baseline for measurements of the flow-structure interaction. The thickness of the rigid panel is 0.7 *in* (17.8 mm).

Thickness [mm]	Mode 1 [Hz]	Mode 2 [Hz]	Mode 3 [Hz]
2	699	946	1351
1.5	524	709	1013
1	349	473	675

Table 3 Compliant panel modal frequencies for each of the 3 panel thicknesses.

Oil surface flow visualizations were done to observe the geometry of the flow in the compression ramp interaction as well as the effects of the presence of a non-rigid floor. Figure 3.2.5 shows the in the rigid panel case, in which the interaction is nominally 2D, and the shock foot, separation and reattachment regions are clearly visible. When the rigid panel was replaced with the 2 mm compliant panel without cavity back-depressurization (i.e., open to atmosphere), the panel bulged into the tunnel, disrupting the flow and creating a much larger separation bubble. When this test was repeated but with the cavity depressurized to near P_∞, the structure of the flow returns to how it looked in the rigid case, thus showing that both the compliance of the floor surface and the pressure difference on the panel certainly have an effect on the structure of the flow interaction.

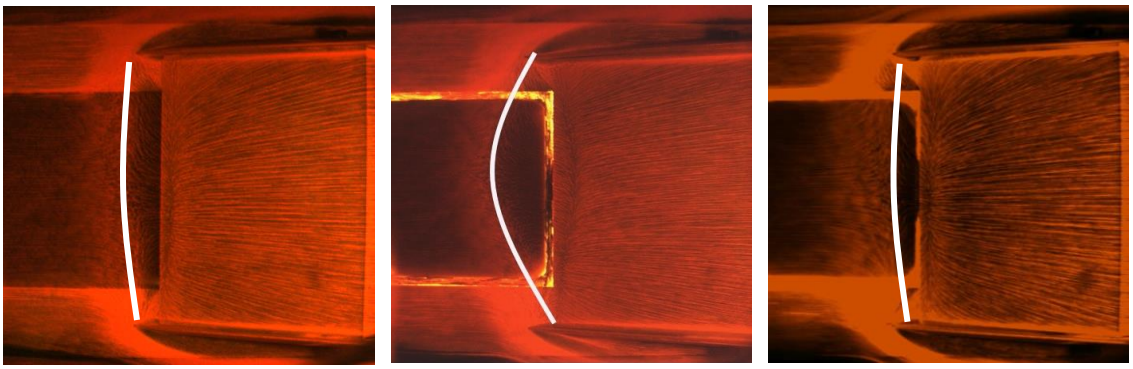

(a) (b) (c)

Figure 27 Surface flow visualizations of 20 degree Mach 2 compression ramp interaction on (a) rigid panel, (b) 2 mm compliant panel with cavity open to atmosphere, and (c) 2 mm compliant panel with cavity depressurized to 7 psi. White line indicates approximate shock foot location

3.3 DATA ACQUISITION SETUP – PRESSURE SENSITIVE PAINT

The PSP was made in-house using a formulation provided by Davis et al. [2015]. The recipe used is for a binary fast-response porous PSP, consisting of an initial polymer-ceramic (PC) substrate binder layer to which a second luminophore layer is then applied. The PC binder mixture was applied to the surface of the test panels using a Zeny™ Model TK-80 air compressor set to 40 psi and with siphon-fed spray gun in a series of single passes, waiting about 30 seconds between each pass, and allowed to cure overnight. It is worth noting that the surface finish or "graininess" of the PC binder layer varied greatly between painting sessions. It is believed that this is likely due to the temperature and humidity of the painting environment as well as the extent to which the paint was homogenized during mixing.

The luminophore layer uses a platinum-tetra-fluoro-phenyl-porphyrin (PtTFPP) luminophore in a solution with methanol. The solution was mixed and kept covered away from light. It was applied to the model using a finer gravity-fed air brush, which allowed greater flow rate control, also applied in a few single passes. Due to the rapid degradation of the paint, the luminophore was not applied until right before testing was to be done. The PSP was illuminated using an LM2xLZ-400 continuous light source from Innovative Scientific Solutions, Inc., and the emission is collected by a FASTCAM Mini AX 200 high-speed camera fitted with a 50 mm lens and a yellow long pass filter. A generic conceptual setup of PSP is shown in Figure 3.3.1, and the installed and painted model in the Mach 2 wind tunnel is shown in Figure 3.3.2.

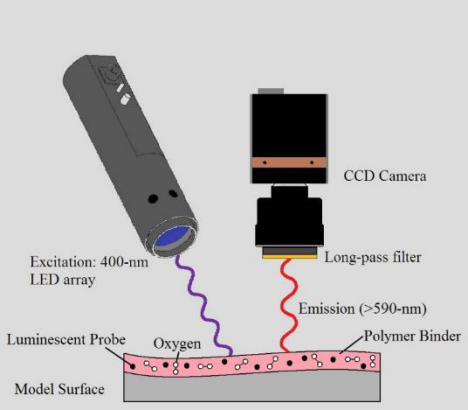

Figure 28 Binary porous PSP concept and setup with 400 nm excitation light and high-speed CCD camera. (Courtesy of Innovative Scientific Solutions Incorporated)

Figure 29 Photograph of the floor of the wind tunnel showing the PSP-painted compliant panel and the compression ramp.

The PSP was first tested on aluminum samples placed in a pressure-controlled box where the luminosity was observed as the pressure was reduced from 1 atm to approximately 3 psia (0.2 atm). In this range, it was found that the intensity change was fairly parabolic in nature with respect to the change in ambient pressure, and a maximum intensity ratio of around 3 was obtained. Figure 3.3.3 displays a calibration curve produced by decreasing the ambient pressure from 13 psi to 3 psi in steps of 1 psi and recording intensity images. The response of the PSP is very closely approximated by a quadratic fit curve.

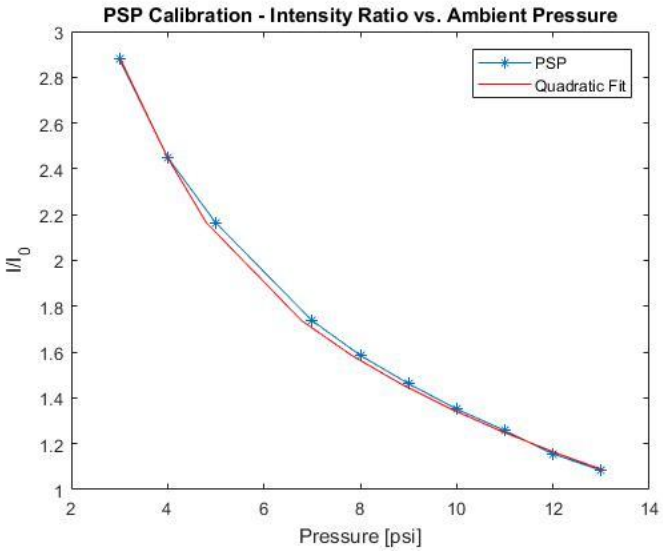

Figure 30 PSP calibration curve for pressures ranging from 3 to 13 psi.

The response of the PSP resolves reliably up to at least 5 kHz (see Section 4.1). During testing, images were acquired at 6.4 kHz and saved onto one computer via a Gigabit Ethernet connection. First, 100 background images without illumination were taken, then the excitation lamp was turned on and 100 wind-off images were taken. These two sets of images were averaged to form a single background and a single wind-off image. Once the tunnel reached steady state, the camera was triggered through a LabView program that in turn triggered the recording of images for the PSP as well as the pressure measurements from the Kulite sensors. The data from the Kulites is read through a National Instruments™ NI TB-4330 8 channel terminal block connected to a PXIe-1073 5-slot chassis data acquisition system, which was then saved onto a second computer. During testing, we had problems with the writing of simultaneous data from the PSP camera and the Kulites onto a single computer, so a second computer was set up to write the data. All of the acquired images from the high-speed PSP camera were dewarped in Matlab after taking an image

with a calibration grid. The uniform grid contained dots of uniform size and pitch, and it was taped over the compliant panel prior to taking wind-off and background images. In processing, the wind-on images were normalized by the wind-off image, with the background subtracted out. Using pressure measurements obtained from the Kulites just upstream of the test panel, the average maximum intensity ratios of the incoming boundary layer could be set to the incoming boundary layer pressure (lowest pressure in the interaction). With this one calibration point, the rest of the field could be linearly mapped to produce a view of surface pressure over the compliant panel. Data and images from the PSP are displayed and discussed in Chapter 4.

3.4 DATA ACQUISITION SETUP – DIGITAL IMAGE CORRELATION

Two cameras were used for stereo DIC. The cameras were positioned underneath the tunnel at an offset angle of approximately 30 degrees from vertical, viewing the underside of the compliant panel through the fused quartz window. The cameras were each fitted with 50 mm lenses. Two Nightstick NSR-1514 1000 lumen brightness LED lights were used to provide lighting on the panel. The cameras were connected to the same voltage trigger as the high-speed PSP camera, so all measurements (incoming boundary layer pressure, panel surface pressure, and displacement) could all be started simultaneously. The images were saved onto a third separate computer.

By using two separate cameras in a stereoscopic configuration with a 60 degree angle offset to capture images, out-of-plane movement of the panel can be detected and

deformation images can be generated. The frame-by-frame movement can be tracked by locating randomly generated “speckles” on the test surface. The DIC concept is shown in Figure 3.4.1, where the movement of a given speckle is tracked from one frame to the next. Figure 3.4.2 provides a view of the underside of an installed panel that had been painted white, then black dots were applied by hand using a fine-tipped marker. Images were acquired at 6.4 kHz, and the cameras allowed for 17,195 images to be taken for a total of 2.69 seconds. The entire panel was able to be captured in the field of view. Prior to data acquisition, a calibration target was installed in place of the compliant panel. The target consists of a uniform dot grid with constant 1.5 mm pitch and 0.75 mm height, shown in Figure 3.4.3. Images were taken at 3 locations in the z direction, which is normal to the floor and the cameras’ plane of view. The locations were at z = -3 mm, z = 0 and z = 3 mm. These images serve to calibrate the DIC to within 0.2 pixels of a fixed known location, providing deformation measurement accuracy.

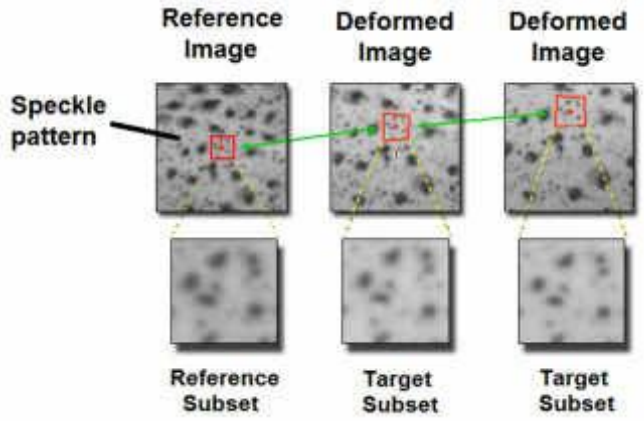

Figure 31 DIC concept of speckle pattern tracking. (Adapted from Guillermo et al. [2017])

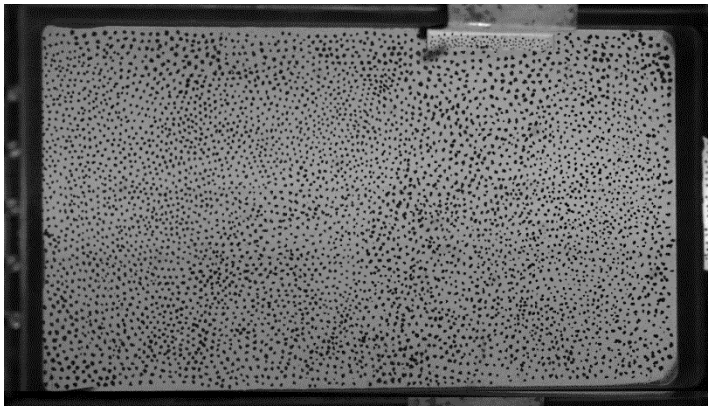

Figure 32 Photograph of the hand-applied speckle pattern on underside of compliant panel for DIC.

Figure 33 Photograph of the installed target grid used for DIC camera calibration.

Once calibrated, extreme care was taken while installing the compliant panel and setting up the remainder of the equipment so as not to bump the cameras. A basic schematic of the DIC and PSP camera setup is shown in Figure 3.4.4. The orange line indicates the compliant panel, located just upstream of the compression ramp. Directly under the panel

is the window cavity. The PSP camera and 400 nm light source point downwards from above, and the LED lights (not shown) and DIC cameras point upwards from below.

The set of images obtained is processed relative to an initial undeformed wind-off case with the cavity open to atmosphere, i.e., with no back-pressure compensation. Each successive image in the dataset indicates the evolution of deformation of the compliant panel relative to the original undeformed case. These results are discussed thoroughly and compared to those obtained from the PSP in Chapter 4.

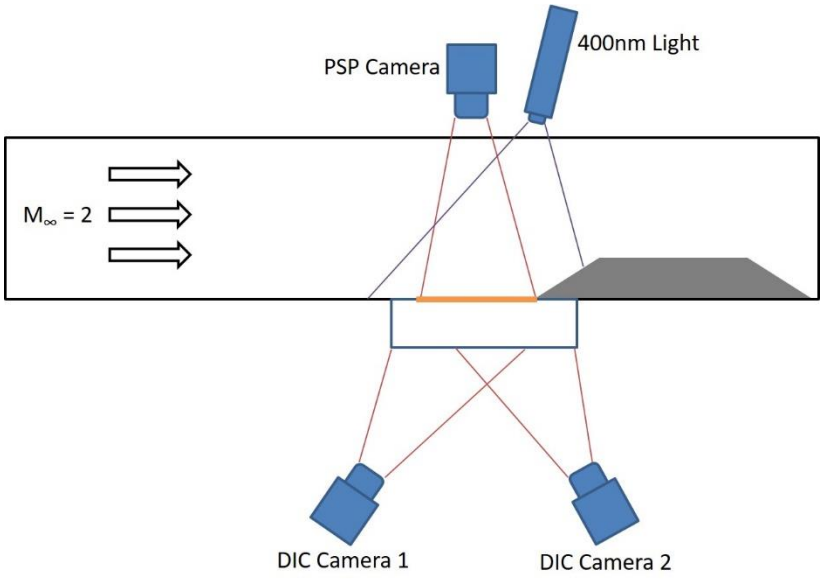

Figure 34 Schematic of PSP and DIC camera setup in the Mach 2 wind tunnel (not to scale).

CHAPTER 4

Results

4.1 SURFACE PRESSURE MEASUREMENTS

The PSP images were acquired at 6400 frames per second for a total of 10,918 images at 1024x1024 resolution, resulting in roughly 1.7 seconds of data. Matlab was used to take the raw images and process them to give a pressure ratio mapping over the field of view. First an intensity ratio was obtained from the wind-on to the wind-off images, and then they were correlated with the incoming boundary layer pressure measured by the upstream Kulites to produce surface pressure. These images were then averaged to create a single mean pressure distribution. Additionally, the image sequences can be combined into a time-resolved video of the unsteady pressure field underneath the interaction. Note that any changes in intensity of the light due to panel deformation are neglected.

Visible in the processed images is the incoming boundary layer, shock foot and separation region. Figure 4.1.1 is an example of the mean PSP intensity ratio for a SWBLI over a 2 mm compliant panel subjected to a 20 degree compression ramp interaction at Mach 2, and Figure 4.1.2 is the ratio mapped to surface pressure. Flow is from left to right, and the ramp is located on the right edge of the figure at $x/\delta_{99} = 0$. Note that due to limited optical access, the field of view as seen by the PSP camera gave only about two-thirds of the full panel area, but this was still enough space to adequately observe the interaction. The approximate cropped field of view was 2 *in* × 3 *in*, as indicated in Figure 4.1.3. This

provided pressure data up to $6\delta_{99}$ in length upstream from the ramp on the panel and $4\delta_{99}$ in the spanwise direction. In these images, owing to quenching of the signal by oxygen, high signal intensity ratio corresponds to low pressure and vice versa. In the figures, the mean shock foot location can clearly be seen beginning at around x/δ_{99} = -2 as the pressure increases across the shock.

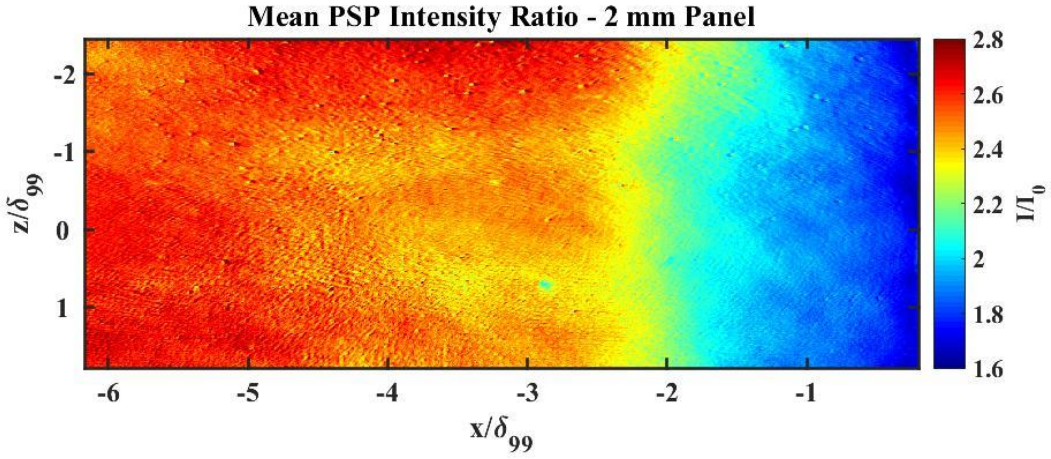

Figure 35 Mean PSP intensity ratio for Mach 2 SWBLI on a 2mm panel.

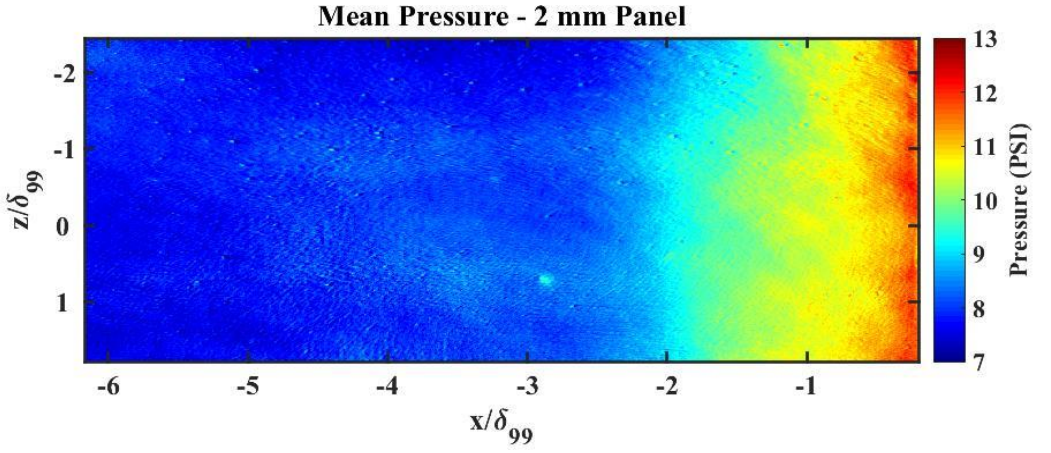

Figure 36 Mean PSP surface pressure distribution for Mach 2 SWBLI on a 2mm panel.

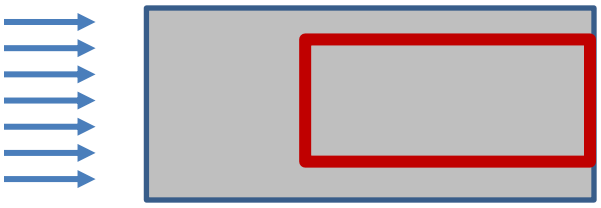

Figure 37 Approximate field of view (red box) of panel as seen by PSP camera. Incoming flow is left to right.

In Figure 4.1.2, the blue region is the free stream, the aqua-colored region is the shock foot, the yellow/orange region is the separation region, and the red region is near the ramp edge. When the frame-by-frame sequence of images is viewed, very prominent, large-scale oscillations in the shock foot position are observed. There are areas of lighter blue, i.e., higher pressure, which appear upstream of the shock foot on the panel, due to unsteadiness. These higher-pressure regions are highlighted by the red circle in Figure 4.1.4, which is a still image taken from during the run. Interestingly, it seemed that the movement of these shadows synchronized with the shock foot, which suggests a coupling between the shock foot and surface pressure. The unsteadiness of the shock foot can be seen in a time sequence of the PSP, as shown in Figure 4.1.5, displaying the pressure variations and the movement of the shock foot.

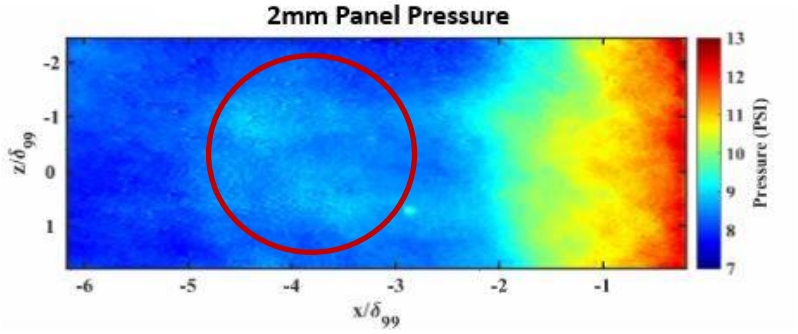

Figure 38 Example image of PSP taken during the tunnel run showing higher pressure (lighter blue color, identified by red circle) appearing upstream of the shock.

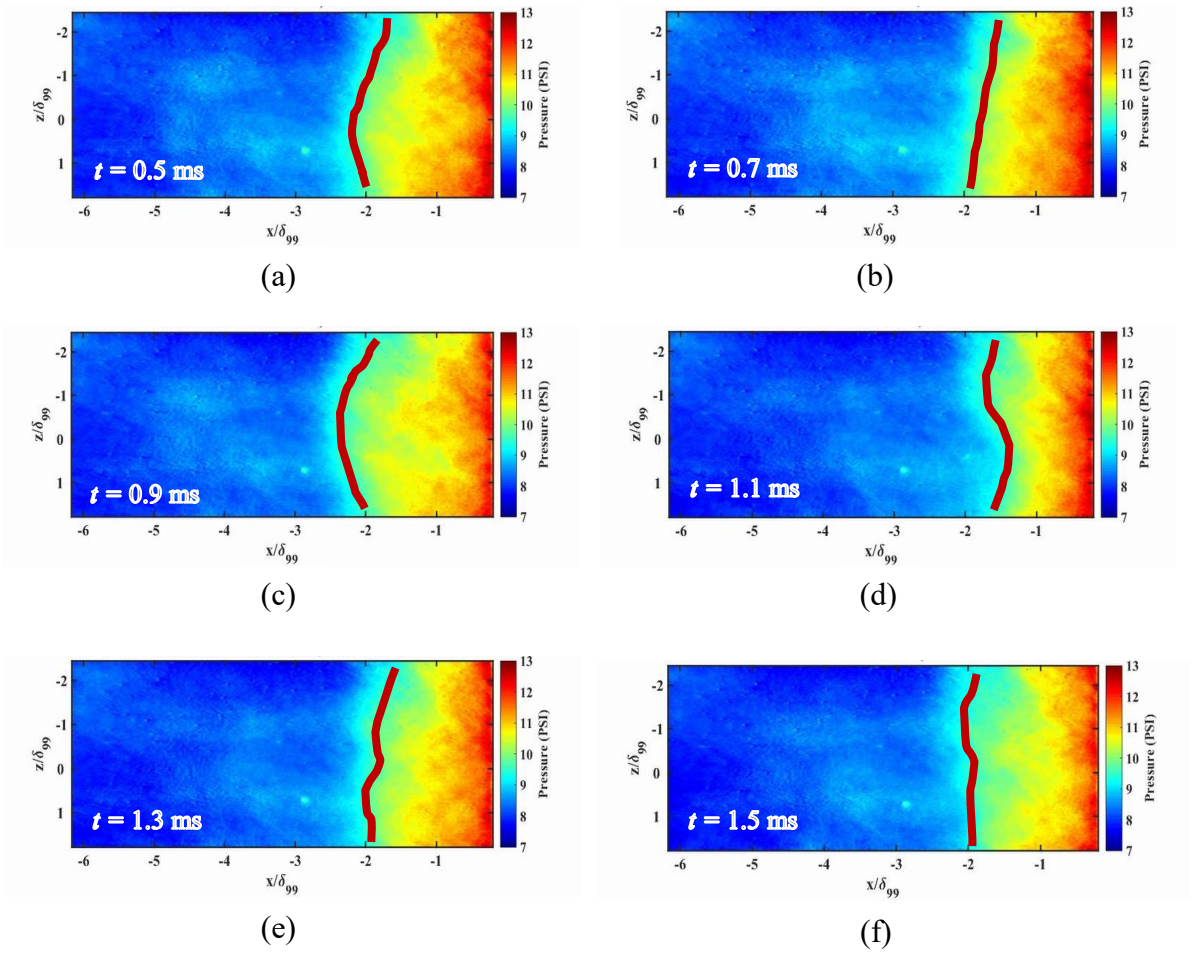

Figure 39 Time sequence of PSP showing surface pressure and shock foot location at (a) t = 0.5 ms, (b) t = 0.7 ms, (c) t = 0.9 ms, (d) t = 1.1 ms, (e) t = 1.3 ms and (f) t = 1.5 ms.

In order to validate the data acquired from the PSP, we compared the PSP response to that of the Kulites in previous experiments run in the same tunnel. An example of the comparison is shown in Figure 4.1.6, where the responses of both the PSP and the Kulites match very well. In Figure 4.1.7, the power spectra are compared at a location under the shock foot in a previously-conducted swept compression ramp test case. It is seen that the

response matches well up until about 5 kHz, where significant roll-off is seen in the PSP. Thus, the PSP is seen as a reliable method of measuring pressure for frequencies up to 5 kHz, which is more than sufficient for resolving shock foot oscillations.

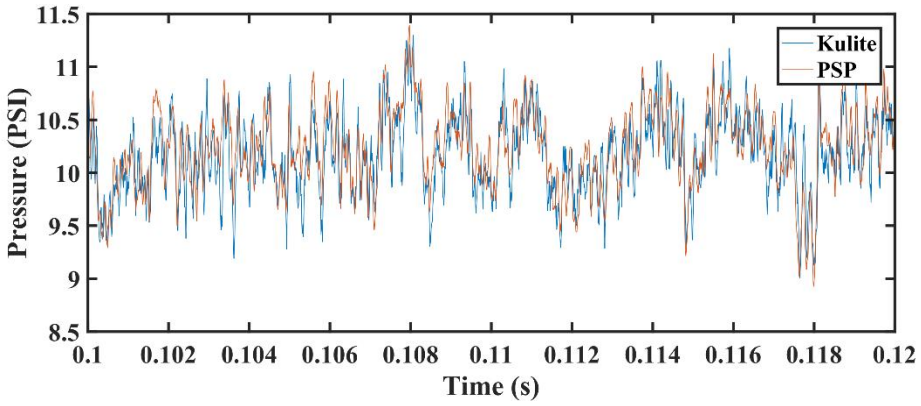

Figure 40 Time series comparison between PSP and a single Kulite for a previously studied swept compression ramp interaction.

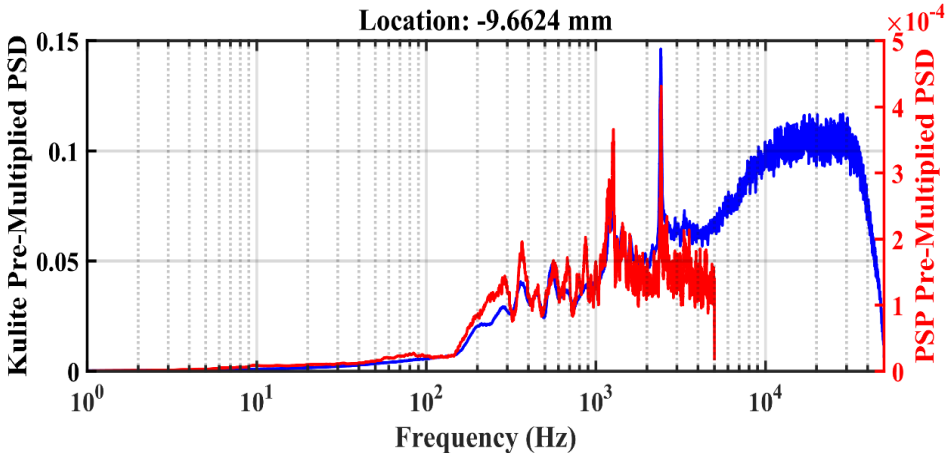

Figure 41 Power spectral density comparison for PSP and a single Kulite under the shock foot of a previously studied swept compression ramp interaction.

4.2 DISPLACMENT MEASUREMENTS

The DIC images were acquired at 6.4 kHz for a total of 17,195 images, resulting in 2.69 seconds of displacement data. The images were recorded into LaVision DaVis software on a separate computer from the ones used to acquire the PSP image and the Kulite pressure measurements. This software was also used to perform all of the analysis for the DIC. The set of all images was appended using a wind-off, undeformed reference image, and each successive image was processed relative to the previous image. Similar to the manner in which the PSP images were processed, all of the images can be averaged together to produce a mean deformation image for the entirety of the recording time. These mean displacements are shown in Figure 4.2.1 for the 2 mm, 1.5 mm and 1 mm panels. Note that the range of the *y* axis values is different for each panel to clearly show the panel mean deflection and that the field of view is approximately the entire surface of the panel, unlike the limited field of view given by the PSP. In Figure 4.2.2, the maximum displacements are shown and the *y* axis scales are adjusted to compare relative magnitudes.

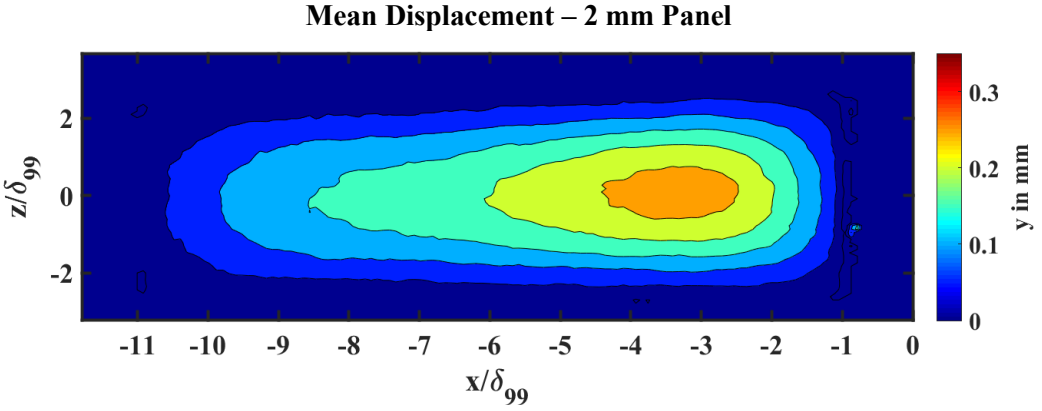

(a)

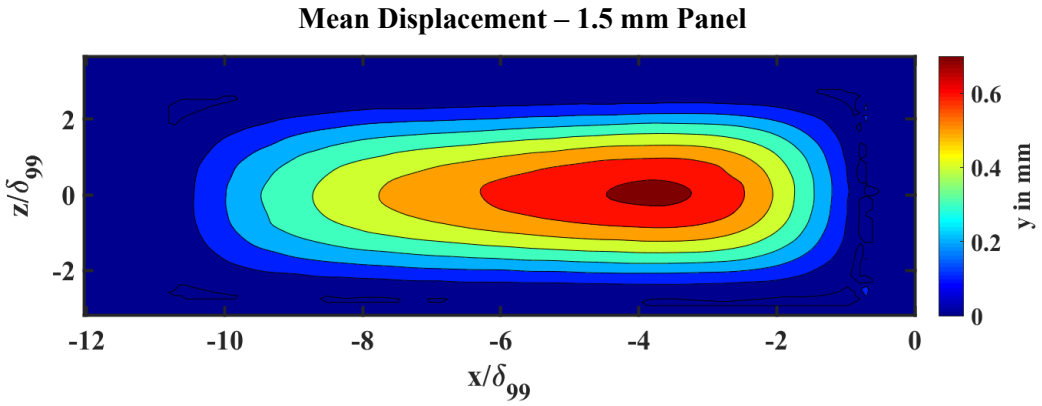

(b)

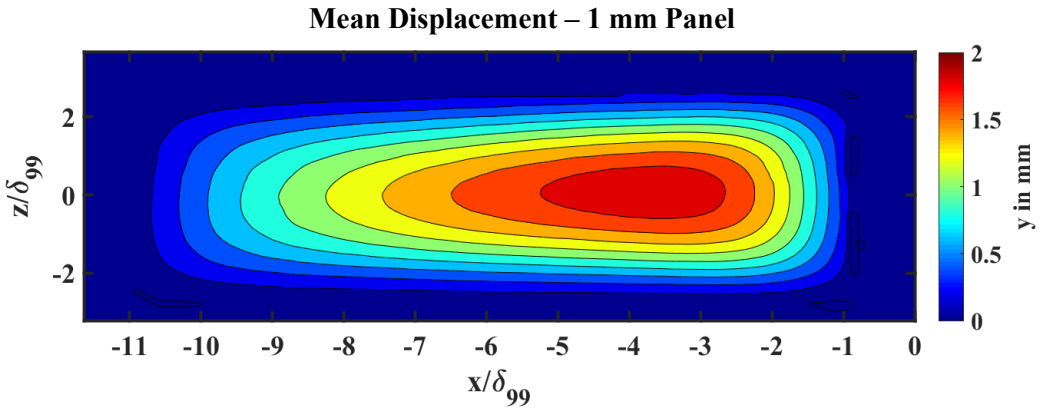

(c)

Figure 42 DIC – Mean displacement for (a) 2 mm panel, (b) 1.5 mm panel and (c) 1 mm panel.

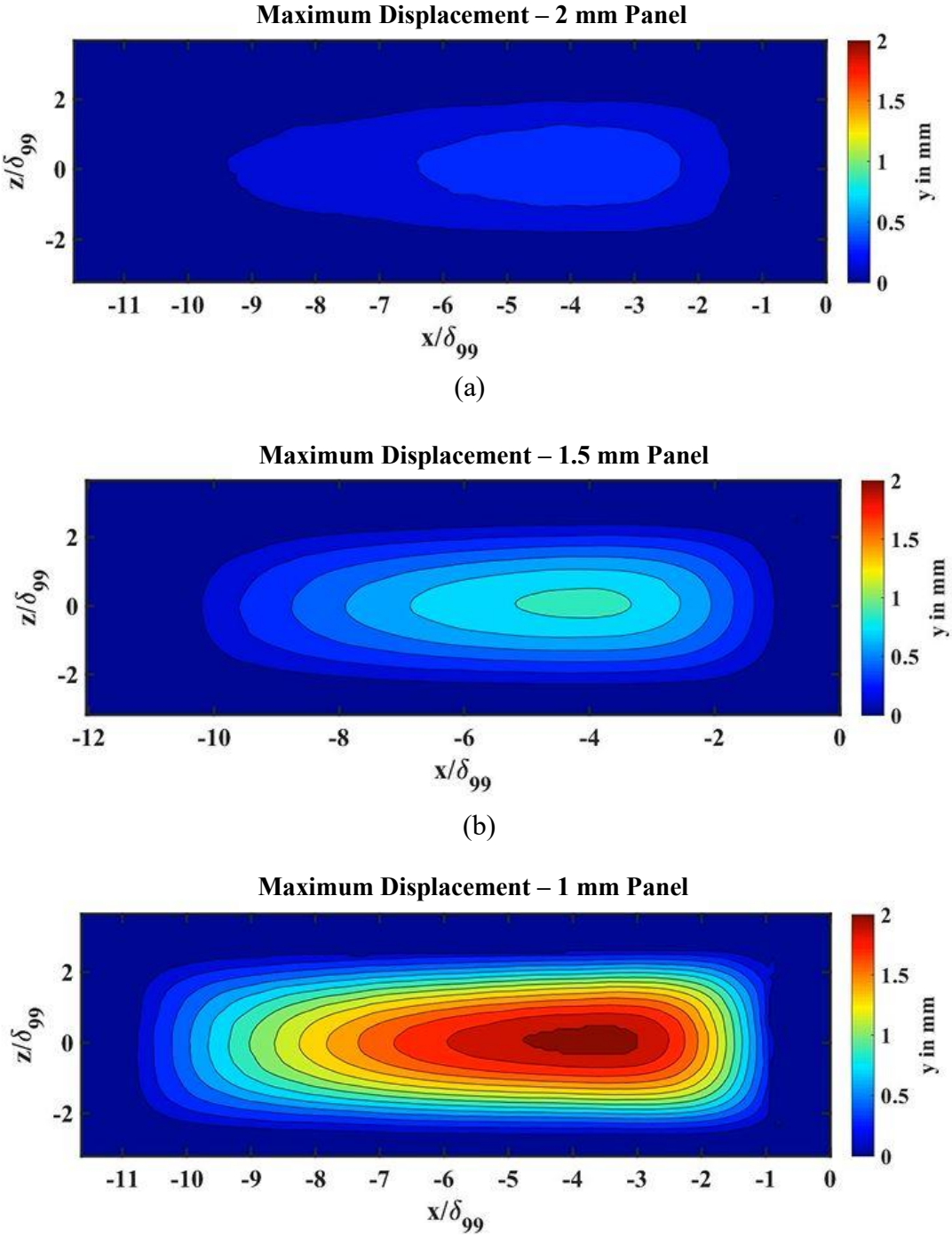

Figure 43 DIC – Maximum displacement for (a) 2 mm panel, (b) 1.5 mm panel and (c) 1 mm panel with constant *y* axis.

It is clear that as the panel thickness decreases, the mean deflection increases (positive *y* direction is downward, into the cavity). For the 2 mm panel, the maximum mean deflection was about 0.25 mm. For the 1.5 mm panel, the maximum mean deflection was about 0.7 mm, and in the 1 mm panel case, the maximum mean deflection was 1.8 mm. Other observations that can be seen are the consistent location of the maximum deflection due to the ramp interaction, which is found on the streamwise centerline on the downstream half of the panel between $3\delta_{99}$ and $4\delta_{99}$ from the ramp edge. This location is just upstream of the beginning of the shock foot, which was at about $2\delta_{99}$ as inferred from the PSP. A comparison between the PSP and DIC will be further discussed in section 4.3.

Time-resolved videos of the panel deflection obtained from the image set also revealed first-mode oscillations in both the magnitude of the deflection and the location of the maximum. There is a visible shift in the center of maximum displacement in the streamwise direction during the tunnel run. Figure 4.2.3 shows an instantaneous local maximum and local minimum deflection at different time steps during a tunnel run with the 1 mm panel. Similar results were obtained for the 2 mm and 1.5 mm panels. These images were taken 9 frames, or 1.4 milliseconds apart. The deflection is at a maximum when the center is further upstream, at around 4 to $4.5\delta_{99}$, and it is at a minimum further downstream, closer to $3\delta_{99}$. Figure 4.2.4 displays a time sequence of the DIC for the 1 mm panel, where the change in panel deflection magnitude as a function of pressure forcing can be seen clearly.

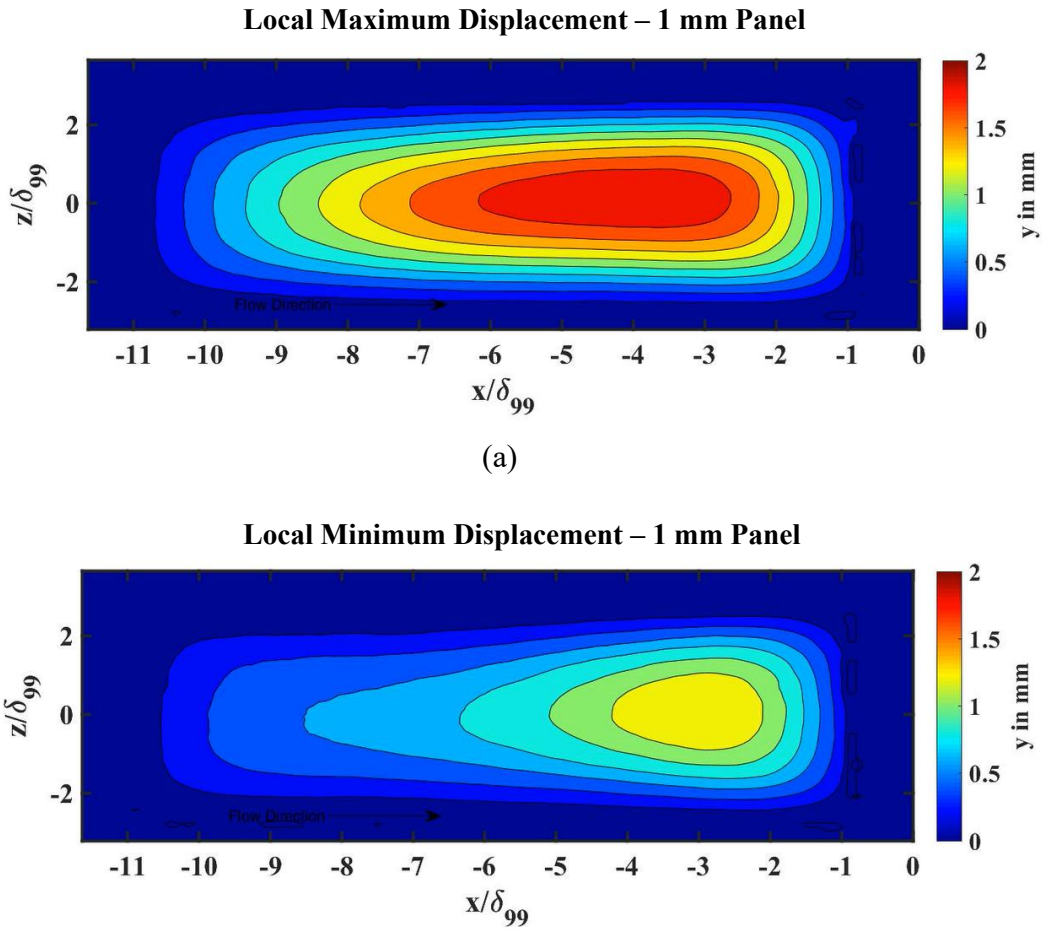

Figure 44 DIC – Instantaneous displacement for 1 mm panel where displacement is at a (a) local maximum and a (b) local minimum 1.4 milliseconds later.

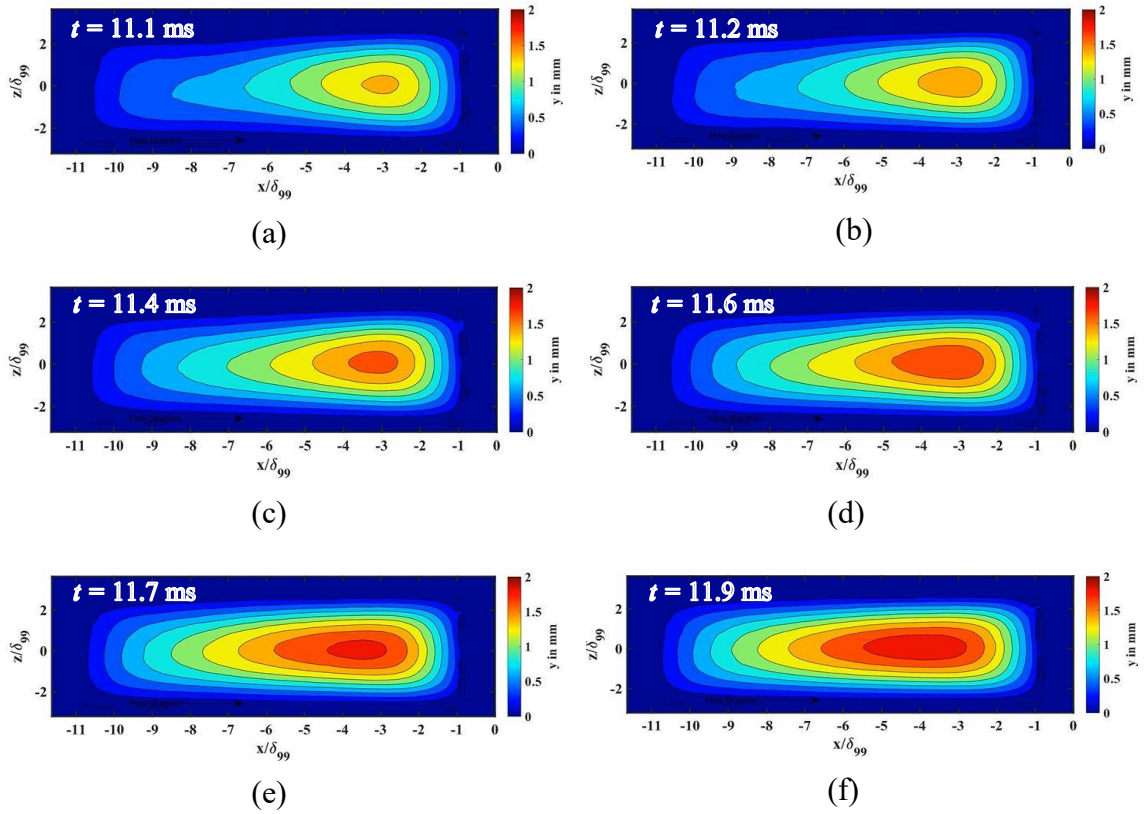

Figure 45 Time sequence of DIC showing displacements at (a) t = 11.1 ms, (b) t = 11.2 ms, (c) t = 11.4 ms, (d) t = 11.6 ms, (e) t = 11.7 ms and (f) t = 11.9 ms.

4.3 COMPARING SIMULTANEOUS SURFACE PRESSURE AND DISPLACMENT MEASUREMENTS

In order to investigate the coupling between the shock foot movement and floor displacement in the fluid-structure interaction, the analysis from the simultaneous PSP and DIC were compared. First, time histories of the recorded PSP and DIC data were analyzed to determine the delay between the onsets of image acquisition from the common 3-way

trigger. The normalized amplitudes for the first 5000 images (about 0.78 seconds) for both sets of images for the 2 mm panel case is shown in Figure 4.3.1. Cross-correlation analysis of the data sets, shown in Figure 4.3.2, revealed a time shift of about 270 microseconds where displacement was leading the pressure, indicating a system where the panel deflects and then subsequently causes a change in the pressure on top of the panel.

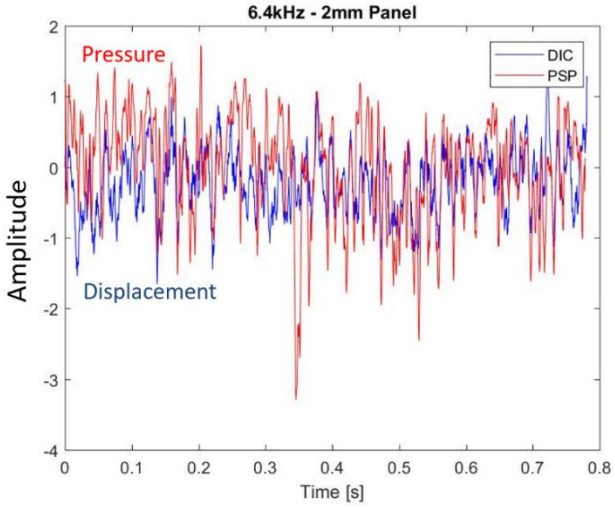

Figure 46 Pressure and displacement time history of first 5000 images for 2 mm panel.

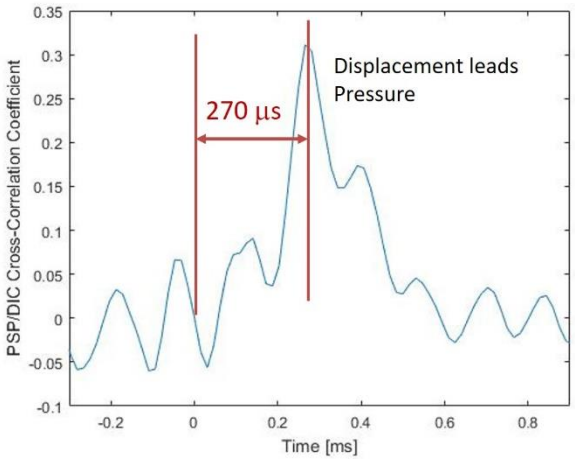

Figure 47 Time lag of pressure and displacement measurements. Displacement leads pressure at peak cross-correlation by 270 microseconds.

From the simultaneous images, we observed a displacement maximum and following minimum and compared them with the corresponding instantaneous surface pressure. At the maximum, the center of deflection is further upstream, indicating the shock foot is located further upstream, resulting in more high pressure past the shock acting on the surface of the panel. In the opposite case, at the minimum, the center is further rearward, indicating the shock has moved downstream and there is less high pressure acting on the panel. A comparison of these images is shown in Figure 4.3.3 and Figure 4.3.4. At t = 5.9 ms, the displacement is at a local minimum at a streamwise location of $x/\delta_{99} \approx -2.8$, and the corresponding frame from the PSP taken after the time lag reveals that the shock foot is near its furthest downstream position at $x/\delta_{99} \approx -1.4$. In contrast, 6 frames later at t = 6.9 ms, the shock foot is further upstream at an average position near $x/\delta_{99} \approx -2$, and a large, curved non-2D bulge of higher pressure appears. This moment of increased separation and higher pressure close to the center of the panel would be expected to yield an increase in deflection magnitude, and the corresponding frame for the displacement indeed shows a local maximum. The location of the maximum also shifts upstream to $x/\delta_{99} \approx -4.8$.

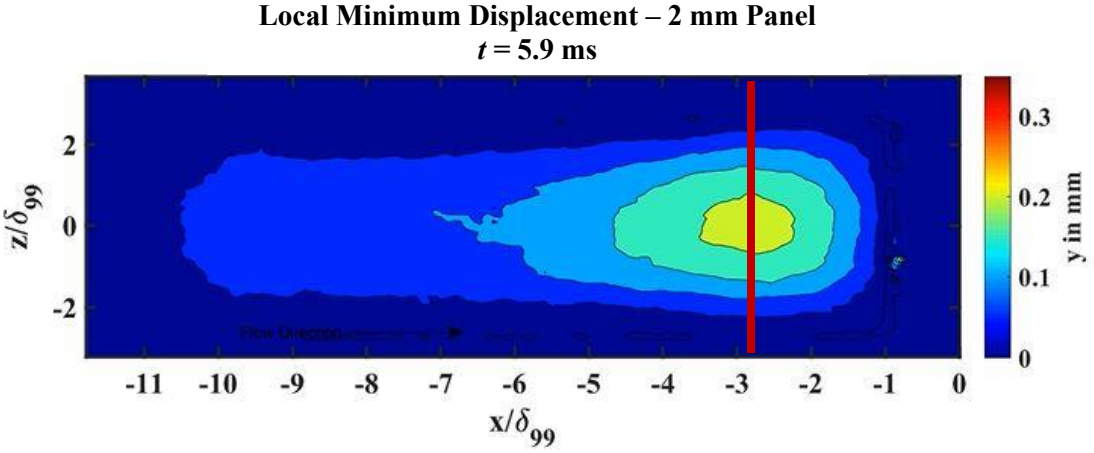

(a)

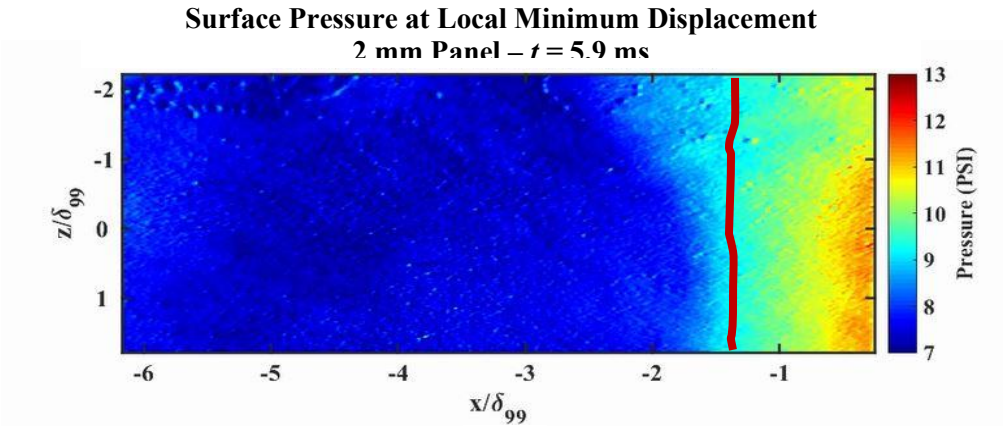

(b)

Figure 48 Instantaneous simultaneous (a) displacement and (b) surface pressure for 2 mm panel at local deflection minimum at time t = 5.9 ms. Red line represents approximate location deflection center and trace of shock foot.

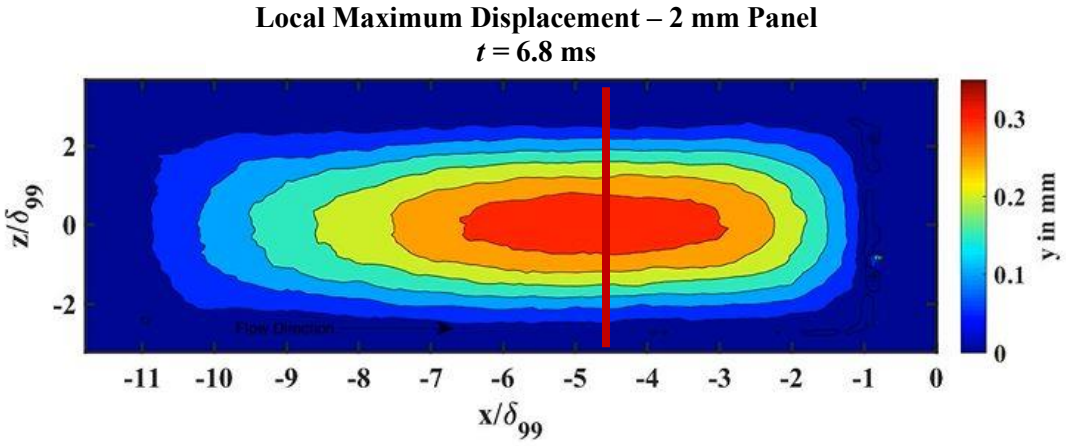

(a)

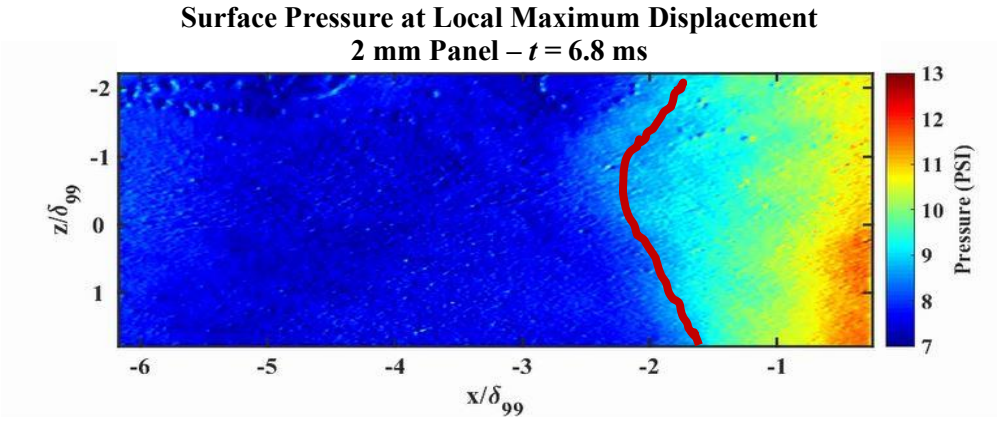

(b)

Figure 49 Instantaneous simultaneous (a) displacement and (b) surface pressure for 2 mm panel at local deflection minimum at time t = 6.8 ms. Red line represents approximate location deflection center and trace of shock foot.

4.4 POWER SPECTRAL DENSITIES

The spectral content of the data was analyzed in order to further investigate the coupling between a compliant surface and the shock foot movement in a SWBLI. The power spectral density of the PSP pressure data was taken at a location on the panel underneath the shock foot. The PSD of the displacement was taken at the same location on the underside of the panel. Lastly, a surrogate shock foot was created to represent the spectral content of the shock foot itself. The surrogate is essentially a pressure contour across the spanwise width of the panel. The spectral content of the 2 mm panel is shown in Figures 4.4.1, 4.4.2 and 4.4.3. The varying added mass of the paint and slight surface

heating are believed to be two main sources of discrepancies of modal peaks in each measurement compared to the theoretically calculated values.

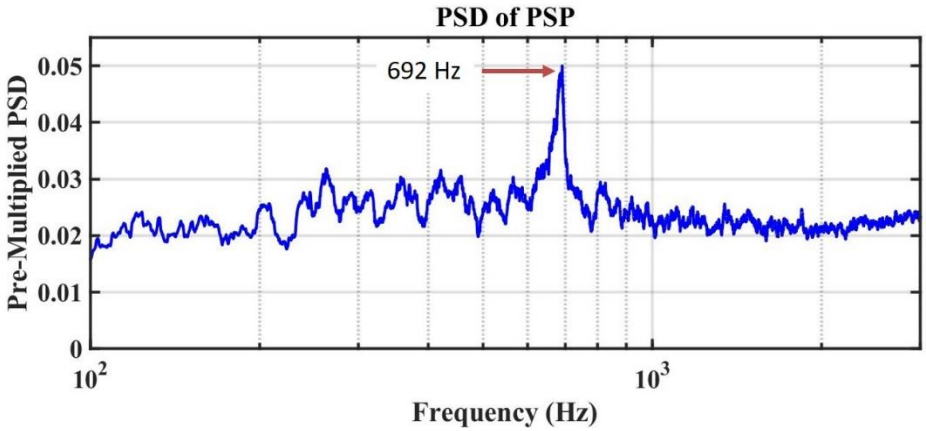

Figure 50 Power spectral density of pressure for 2 mm panel with first mode labeled.

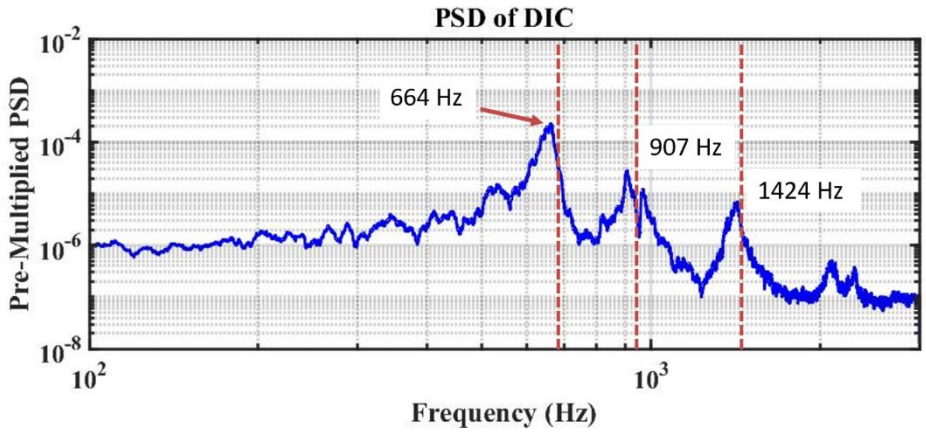

Figure 51 Power spectral density of displacement for 2 mm panel with first 3 modes labeled. Dotted red lines indicate theoretical values

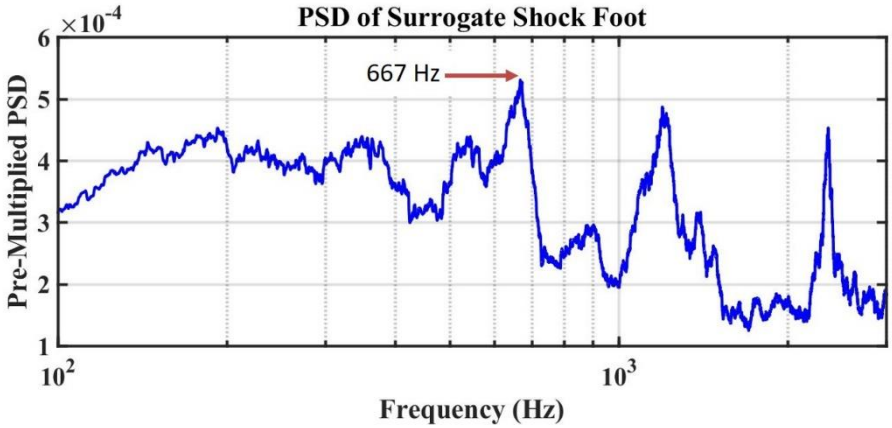

Figure 52 Power spectral density of surrogate shock foot for 2 mm panel with first mode labeled.

In Figure 4.4.1, a distinct peak is found at 692 Hz, which is very near the calculated theoretical value of 699 Hz – a difference of 1.0 percent. From previous studies in the same wind tunnel, we have found that there is very little mid-frequency content in the boundary layer, so it can be determined that the peak is in fact due to the presence of the compliant panel and is not intrinsic to the tunnel. After a series of tests, it seemed that the PSP resolved the first mode of the panel quite well, however was not able to consistently pick up the second and third modes very well. The first mode also contains the most energy in the interaction, so it is of most importance compared to secondary modes and is the focus of the spectral analysis.

In Figure 4.4.2, the DIC can be seen to resolve the first 3 modal frequencies very well, with each successive peak decreeing slightly in magnitude. These frequencies are at 664 Hz, 907 Hz and 1424 Hz, respectively, giving an average deviation from the theoretical values (red dotted lines) of 4.84%. Note that the peak at ~2.3 kHz is not characteristic of

the panel compliance; it is related to electrical interference or an acoustic mode of the wind tunnel.

In Figure 4.4.3, the surrogate shock foot also gives a frequency peak near the first mode at 667 Hz. Akin to the PSP content, the first mode resolves the best and has the most energy. These PSD analyses were repeated for the 1.5 mm and 1 mm panels and yielded similar qualitative results. Shown in Figure 4.4.4, the PSDs for each of the three panels are compared. In Figure 4.4.4 (a), the previously discussed results for the 2 mm panel are shown again. In Figure 4.4.4 (b), the modal frequency peaks in the PSP, DIC and surrogate shock foot all shift down towards the lower natural frequency of the thinner 1.5 mm panel. The first mode is at 524 Hz, and the PSDs give frequencies of 522 Hz, 566 Hz and 550 Hz. Figure 4.4.4 (c) shows the same for the 1 mm panel, where the first mode is 349 Hz, and frequencies of 412 Hz, 435 Hz and 432 Hz. The larger difference from theory for the 1 mm could possibly be due to its excessive compliance. When the cavity was depressurized, it caused the panel to deflect downward into the cavity so much that the “rigid” sides began to buckle inward, leaving large gaps between the edge of the panel and the tunnel floor. Another observation that was made is the increase in magnitude of the peak as the panel thickness is decreased. The peaks become more pronounced as they have a higher relative energy content.

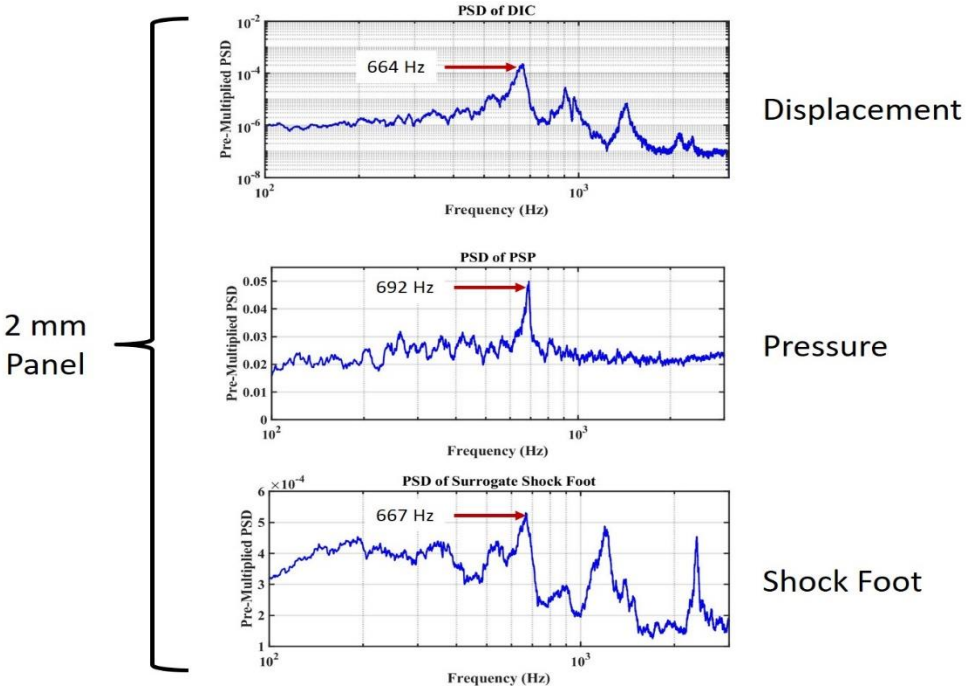
2 mm
Panel
PSD of DIC
664 Hz
Pre-Multiplied PSD
Frequency (Hz)
Displacement
PSD of PSP
692 Hz
Pre-Multiplied PSD
Frequency (Hz)
Pressure
PSD of Surrogate Shock Foot
667 Hz
Pre-Multiplied PSD
Frequency (Hz)
Shock Foot

(a)

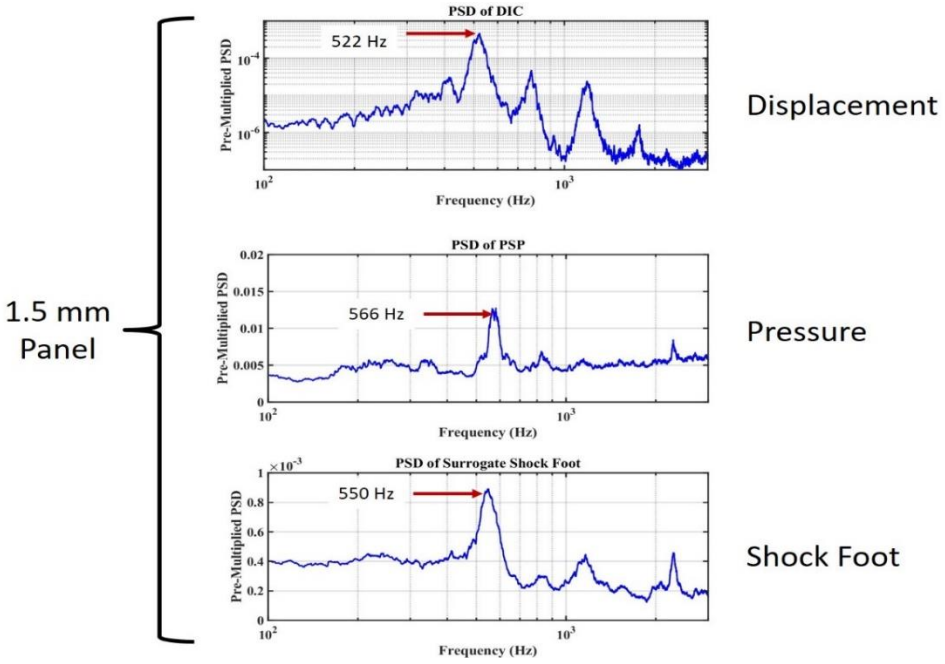

(b)

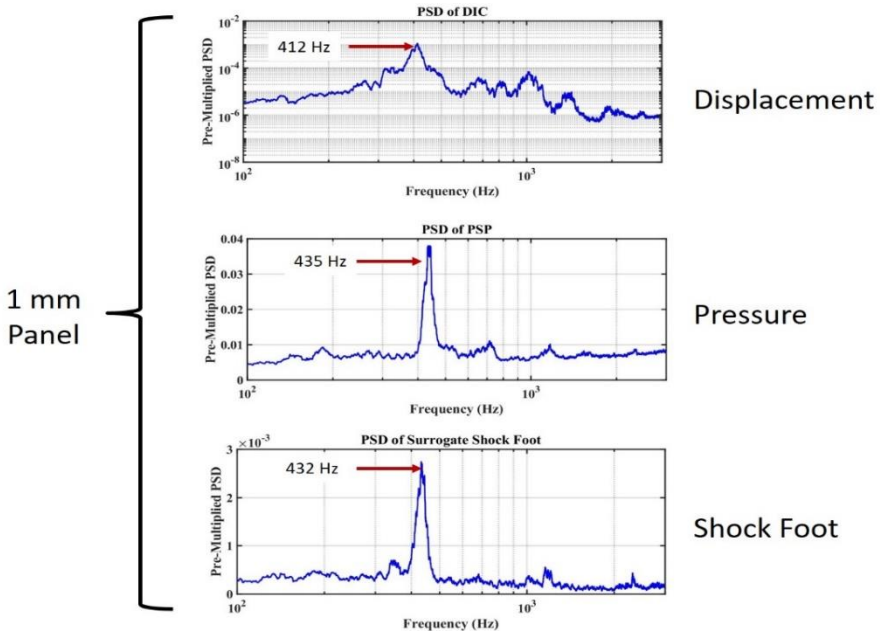

(c)

Figure 53 Comparing power spectral densities of displacement, pressure and surrogate shock foot for (a) 2 mm panel, (b) 1.5 mm panel and (c) 1 mm panel.

The similarity in the panel displacement first-mode frequency and the dominant shock foot oscillation frequency indicates that the compliance of the panel causes the shock foot to respond at the panel's natural frequency. Within the amplification range, the shock foot oscillation frequency seems to lock in to the primary mode of the panel. This is indicative of the hypothesized two-way coupling between the flow and the compliant structure that is present in the SWBLI.

CHAPTER 5

Conclusions

An experimental study was conducted that investigated the dynamic response of a compliant panel undergoing forcing by a compression ramp SWBLI. The primary diagnostics used were PSP and DIC to obtain the surface pressure and panel displacement, respectively. The SWBLI was generated by a 20 degree unswept compression ramp in a Mach 2 flow, and the separation shock foot was located over the downstream third of the panel. A sealed cavity underneath the panel allowed for backpressure control to minimize mean deflections due to the pressure difference between the flow and the room. High-speed surface pressure on the panel was measured using fast-response porous pressure-sensitive paint at 6.4 kHz, incoming boundary layer pressure was measured at 100 kHz using Kulite pressure transducers, and panel deformation was measured using stereo digital image correlation at 6.4 kHz. All data was acquired simultaneously, allowing for adequate comparison of instantaneous pressure and deformation measurements. A comparison between the fast PSP and Kulite measurements, showed that the PSP exhibited a frequency response of about 5 kHz.

Several observations were made from the analysis of the simultaneous time-resolved pressure and displacement data. The PSP and DIC images showed correlations between the fluctuations of the surface pressure and the oscillations of deflection magnitude of the panel. The shock foot movement over the panel produced moments of minimum and maximum deflection, which in turn affected the structure of the flow. When

the deflection was at a local maximum, the shock foot was located further upstream and corresponded to an increase of pressure on the panel and a larger separation region behind the shock. The opposite is true for a local minimum deflection.

It was also found that the shock foot oscillation frequency matched the panel primary modal frequency of the panel. The power spectral densities of the shock foot, panel pressure and panel displacement all yielded energy peaks near the same matching frequency. When the panel thickness was decreased, and thus the first modal frequency also decreased, the shock foot oscillation frequency also decreased and agreed well with the panel modal frequency. Another observation from the PSDs is that the magnitude of the relative energy content near the modal frequencies increases with the thinner panels.

From this study, a moderate correlation between pressure and displacement time histories revealed some degree of coupling between the shock foot and the flexible panel response in a Mach 2 compression ramp interaction. Future work will include implementing simultaneous particle image velocimetry in order to obtain boundary layer velocity measurements along with pressure and displacement, continuing to improve upon PSP recipes and application, and repeating experiments at Mach 5.

References

1. Beardsell, G., Lawson, J., Neet, M., 2016, “Measuring Compliant Surface Motion for Fluid-Structure Interaction in Supersonic Flow”, Submitted.

2. Blevins, R.D., 1979, “Formulas for natural frequencies and mode shape”, Van Nostrand Reinhold Company, USA.

3. Brouwer, K.R., Gogulapati, A. and McNamara, J.J., 2017, “Interplay of Surface Deformation and Shock-Induced Separation in Shock/Boundary-Layer Interactions”, AIAA Journal, vol. 55, no. 12, pp. 4258-4273.

4. Casper, K.M., Wagner, J.L, Beresh, S.J., and Spillers, R.W., 2016, “Unsteady Pressure Sensitive Paint Measurements of Resonance Properties in Complex Cavities”, AIAA Paper 2016-3315.

5. Clemens, N.T., and Narayanaswamy, V., 2014, “Low-Frequency Unsteadiness of Shock Wave Turbulent Boundary Layer Interactions”, Annual Review of Fluid Mechanics, vol. 46, no. 1, pp. 469-492.

6. Daub, D., Willems, S., and Gülhan, A., 2016, “Experiments on the Interaction of a Fast-Moving Shock with an Elastic Panel”, AIAA Journal, vol. 54, no. 2, pp. 670-678.

7. Davis, T., et al., 2015, “Investigation of impinging jet resonant modes using unsteady pressure-sensitive paint measurements”, Exp. Fluid, vol. 56, no. 5, pp. 1-13.

8. Dussauge, J., Dupont, P., and Debiève, J., 2006, “Unsteadiness in shock wave boundary layer interactions with separation”, Aerospace Science and Technology, vol. 10, no. 2, pp. 85-91.

9. Gaitonde, D.V., 2015, “Progress in shock wave/boundary layer interactions”, Progress in Aerospace Sciences, vol. 72, pp. 80-99.

10. Lynch, K.P., Jones, E.M., and Wagner, J.L., 2018, “Simultaneous PSP and DIC measurements for fluid-structure interactions in a shock tube”, AIAA Paper 2018-3870.

11. Martos, J.F.A., et al., 2017, “Experimental Investigation of Brazilian 14-X B Hypersonic Scramjet Aerospace Vehicle”, International Journal of Aerospace Engineering, vol. 17.

12. McNamara, J.J., and Friedmann, P.P., 2011, “Aeroelastic and Aerothermoelastic Analysis in Hypersonic Flow: Past, Present, and Future”, AIAA Journal, vol. 49, no. 6, pp. 1089-1122.

13. Peng, D., Jiao, L., Sun, Z., Gu, Y., and Liu, Y., 2016, “Simultaneous PSP and TSP measurements of transient flow in a long-duration hypersonic tunnel”, Experiments in Fluids, vol. 57, no. 12, pp. 1-16.

14. Pham, H.T., Gianikos, Z.N., and Narayanaswamy, V., 2018, “Compression Ramp Induced Shock-Wave/Turbulent Boundary-Layer Interactions on a Compliant Material”, AIAA Journal, vol. 56, no. 7, pp. 2925-2929.

15. Spottswood, S., Eason, T., and Beberniss, T., 2012, “Influence of shock–boundary layer interactions on the dynamic response of a flexible panel”, in: Proceedings of the ISMA Biennial Conference on Noise and Vibration Engineering, Leuven, Belgium, pp. 603-616.

16. Verma, S.B., Manisankar, C., and Raju, C., 2012, “Control of shock unsteadiness in shock boundary-layer interaction on a compression corner using mechanical vortex generators”, Shock Waves, vol. 22, no. 4, pp. 327-339.

17. Visbal, M., 2014, “Viscous and inviscid interactions of an oblique shock with a flexible panel”, Journal of Fluids and Structures, vol. 48, pp. 27-45.

18. Visbal, M.R., 2012, “On the interaction of an oblique shock with a flexible panel”, Journal of Fluids and Structures, vol. 30, pp. 219-225.

19. Wagner, J.L., et al., 2017, “Preliminary Investigation of Cavity Sidewall Effects on Resonances Dynamics using Time-Resolved Particle Image Velocimetry and Pressure Sensitive Paint”, AIAA Paper 2017-3126.

20. Whalen, T.J., Kennedy, R.E., Laurence, S.J., Sullivan, B., Bodony, D.J. and Buck, G., 2019, “Unsteady Surface and Flowfield Measurements in Ramp-Induced Turbulent and Transitional Shock-Wave Boundary-Layer Interactions at Mach 6”, AIAA Paper 2019-1127.

21. Xiaolin, L., Shihe, Y., Haibo, N., and Xinhai, Z., 2018, “Experimental Investigation on the Unsteadiness in Shock Wave/Boundary Layer Interaction”, Fluid Dynamics, vol. 53, no. 6, pp. 824-834.

Vita

Thomas (Tom) Joseph Goller was born in Staten Island, New York in 1995. In 2004, he moved to Bethlehem, Pennsylvania, where he attended Freedom High School. Upon graduation in 2013, he began secondary education at the State University of New York at Binghamton, where he studied Mechanical Engineering and graduated Cum Laude. In 2017, he continued his education at The University of Texas at Austin, completing a Master's of Science in Aerospace Engineering in 2019. In his spare time, Tom enjoys playing volleyball with friends, playing golf with his father, traveling and cooking. Currently he is planning to obtain a full-time engineering position in industry where he can continue pursuing his love of aerospace.

Email address: Tgoller95@gmail.com

This dissertation was typed by Thomas J. Goller